



TECHNISCHE
UNIVERSITÄT
WIEN
Vienna University of Technology

Fakultät für Physik

DIPLOMARBEIT

**Influence of neutron irradiation on the
structural and superconducting properties of
 Nb_3Sn**

Ausgeführt am Atominstitut - Tieftemperaturphysik und Supraleitung

Unter der Leitung von

Dr. Michael EISTERER

durch

Barbora BUDINSKÁ

Wien, 09.2019



Die approbierte gedruckte Originalversion dieser Diplomarbeit ist an der TU Wien Bibliothek verfügbar.
The approved original version of this thesis is available in print at TU Wien Bibliothek.

Acknowledgement

This master thesis came to life with the kind support and help of many individuals. I would like to express my sincere gratitude to all of them.

Firstly, I would like to thank my supervisor Michael Eisterer for his patience, kind words, help and guidance during my research. His ability to keep a cool head and a positive attitude, and the ability to find a quick solution to for me otherwise stressful situations, is something I wish I will be able to take away with me into my upcoming years.

I would like to thank the rest of the team in the low temperature physics and superconducting department for helping me out around the lab, especially a big thanks goes to the now former member Thomas Baumgartner, who introduced me to the topic of the thesis and helped me get started.

In addition, a thank you to Stephan Pfeiffer from the USTEM department Wien, and Dipl. Dr. Klaudia Hradil and DI Werner Artner from the X-ray center Wien for their cooperation.

Special thanks goes to my entire loving family for their support, and to my beloved friends, that always hear me out, help me relax and unwind.

The biggest thank you goes out to my kind parents. The people that cheered me on during my entire studies, encouraged me to work harder, but also encouraged me to take breaks when I needed them. Thank you for all the times you were there for me when I got overwhelmed with stress. Thank you for always being interested in what I do and always giving me your insight into the current situation, or my work.



Die approbierte gedruckte Originalversion dieser Diplomarbeit ist an der TU Wien Bibliothek verfügbar.
The approved original version of this thesis is available in print at TU Wien Bibliothek.

Abstract

The superconducting material Nb₃Sn is replacing the superconducting material NbTi in focussing and bending magnets of colliders. This will ensure a higher luminosity and higher collision energies in the newly developed colliders. The magnets are however exposed to radiation at the collision points, and Nb₃Sn's high sensitivity to radiation exposure asks for detailed studies on the ongoing changes with radiation and the possible annealing recovery of these changes to plan the necessary shielding and maintenance for the magnets. A powder and a bulk sample of Nb₃Sn were neutron irradiated up to a fluence of $8.31 \cdot 10^{17}$ n/cm² and $1.77 \cdot 10^{18}$ n/cm² respectively and subsequently isochronally annealed up to 900°C. The influence of these processes on the lattice, the transition temperature T_C , the upper critical field B_{C2} , the penetration depth λ and the critical current density J_C is investigated. Different behavior is observed upon annealing for the bulk and powder sample, that was attributed to the sample surface size and/or to the final fluence value. Experiments showed defects present before irradiation. After annealing, their possible disappearance gave rise to superconducting properties with values above the values for the unirradiated samples. The irradiation induced defects responsible for the critical temperature decrease and the critical current density increase are discussed based on the annealing experiments.

Kurzfassung

Das supraleitende Material Nb₃Sn soll das supraleitende Material NbTi in Fokussierungs- und Ablenkmagneten von Beschleunigern ersetzen. Dies wird eine höhere Luminosität und höhere Kollisionsenergien in den neu entwickelten Beschleunigern sicherstellen. Die Magnete sind jedoch an den Kollisionspunkten starker Strahlung ausgesetzt, und die Empfindlichkeit von Nb₃Sn gegenüber Strahlung erfordert detaillierte Studien über die Änderungen der supraleitenden Eigenschaften durch die Strahlung und eine mögliche Wiederherstellung der ursprünglichen Eigenschaften durch eine thermische Behandlung um die erforderliche Abschirmung und Wartung der Magnete zu planen. Eine Pulverprobe und eine Massivprobe von Nb₃Sn wurden mit schnellen Neutronen auf eine Fluenz von $8.31 \cdot 10^{17} \text{ cm}^2$ und $1.77 \cdot 10^{18} \text{ cm}^2$ bestrahlt. Danach folgten thermische Behandlungen mit Temperaturen bis zu 900°C. Der Einfluss dieser Glühungen auf das Gitter, die kritische Temperatur T_C , das obere kritische Feld B_{C2} , die Eindringtiefe λ und die kritische Stromdichte J_c wurde im Rahmen dieser Diplomarbeit untersucht. Nach den Glühungen wird für die Massiv- und die Pulverprobe ein unterschiedliches Verhalten beobachtet, das auf die Probengeometrie und/oder die unterschiedlichen Fluenzen zurückgeführt werden kann. Röntgenbeugung zeigte die Anwesenheit von Defekten schon vor der Bestrahlung. Ihr allfälliges Verschwinden führte nach dem Glühvorgang zu einer supraleitenden Übergangstemperatur oberhalb der Werte für die unbestrahlten Proben. Die strahlungsinduzierten Defekte, die für eine Abnahme der kritischen Temperatur und eine Zunahme der kritischen Stromdichte verantwortlich sind, werden auf der Grundlage der durchgeführten Glühversuche diskutiert.

Contents

1	Introduction	1
2	Theoretical background	2
2.1	Superconductivity	2
2.1.1	Meissner-Ochsenfeld Effect	3
2.1.2	Quantization of the magnetic flux inside a superconductive ring	4
2.1.3	Jump in specific heat C	5
2.1.4	Energy gap	6
2.1.5	Isotope effect	7
2.2	Classification of superconductors	7
2.2.1	Critical current density	8
2.3	Nb_3Sn	9
3	Radiation induced and annealing effects on A15 superconductors	11
3.1	Lattice parameter, long range order parameter and mean displacement amplitude	11
3.2	Critical temperature	12
3.2.1	Reordering kinetics of disordered A15 compounds	15
3.3	Upper critical field	18
3.4	Penetration depth	19
3.5	Critical current density	20
4	Experimental methods	22
4.1	Sample preparation and description	22
4.2	Irradiation and annealing process	24
4.3	X-ray diffraction	25
4.4	SQUID MPMS	26
4.4.1	Critical Temperature	28
4.4.2	Upper critical field	29
4.4.3	Penetration depth	31
4.4.4	Critical current density	33
5	Results and discussion	37
5.1	X-ray diffraction	37

5.2	Critical Temperature	39
5.3	Upper critical field	46
5.4	Penetration depth	49
5.5	Critical current density	51
6	Conclusion	55
	References	60
A	Superconducting properties of Nb₃Sn as functions of Sn content	61
B	SQUID	62

1 Introduction

The superconducting material Niobium-tin Nb_3Sn was discovered already in the year 1954, but only a couple years ago the material became the center of interest and many intensive studies on the material were performed. The reason behind it is the ongoing upgrade project in CERN to build a new High-Luminosity Large Hadron Collider (HL-LHC) [2, 3], and the design development of the Future Circular Collider (FCC). The goal of HL-LHC is to higher the luminosity to 5-times its previous value. New superconducting quadrupole magnets in the hadron collider, that focus the particle beams before they meet, should be able to produce fields up to 12 Tesla. The FCC (the hadron version: FCC-hh) project on the other hand aims to higher the collision energy to 100 TeV from the previous 13 TeV, and requires 16 Tesla dipole bending magnets.

Previously these magnets were made from Niobium-titanium $NbTi$, but since $NbTi$ is only capable of producing magnetic fields up until 9-10 Tesla, search for new materials was set off. Already in the year 1961 Nb_3Sn was found to be able to exhibit superconductivity at high magnetic fields, making it a great candidate and the development of the new magnets could start. During the development process several problems came up. The two main ones being that Nb_3Sn in its superconducting phase is way too brittle to be shaped into cables and Nb_3Sn superconducting properties are being changed after irradiation. The first problem is being resolved by making the cables and winding them into a coil in its unreacted, non-superconducting phase and only afterwards undergoing a heat treatment, that causes a reaction, switching the material to its reactive phase. The second problem, due to the fact that these magnets are going to be exposed to radiation at the collision points, can not be overlooked. To help better understand how the changes in superconducting properties are happening and how to better avoid them, is the main subject of this thesis. Experiments measuring the superconducting properties of the material are performed after several irradiation steps, to establish the exact changes at the exact radiation doses. Following the experiments after the irradiation steps, are the experiments after several annealing steps. The idea behind this, is to get a better idea about the exact defects being created during irradiation, as well as information about the possible recovery of the superconducting properties. All together this information will be useful for the development of the HL-LHC and FCC-hh magnets, its necessary shielding and further maintenance. Information about the created defects can also provide information about how atomic ordering effects superconductivity.

2 Theoretical background

2.1 Superconductivity

The movement of electric charges within a material is determined through scattering on phonons, impurities or on oneself. A very good approximation of the final result for electric resistivity ρ is given by the Matthiessens rule, that states that the electric resistivity of the individual processes can be simply added. In metals however the phonon part outweighs all the other processes at ambient temperature. To describe the phonon part the Bloch-Grüneisen model (figure 2.1) can be applied. In this model, the electrical resistivity grows with temperature and can be split at the Debye temperature into two parts with different behaviors - a high temperature part proportional to T and a low temperature part proportional to T^5 , that converges to a temperature-independent resistivity caused by impurities: $\rho(T=0K)=\rho_0$.

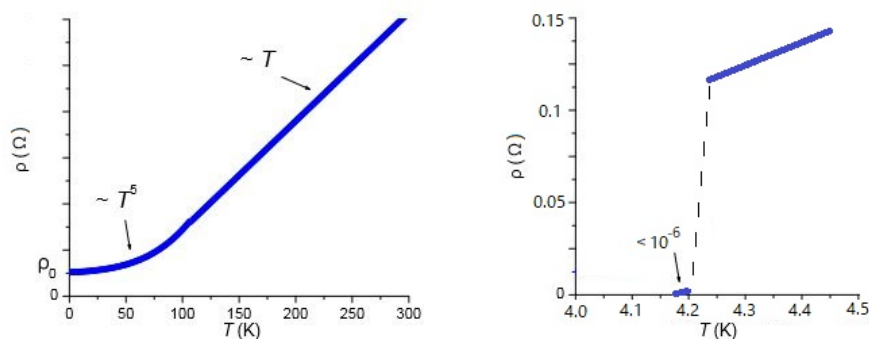


Figure 2.1: Left: Electric resistivity for simple metals as described by the Bloch-Grüneisen model. Right: Electric resistivity of mercury

In the year 1911 Kamerlingh Onnes discovered an unexpected behavior of the electrical resistivity whilst performing measurements on mercury. He observed that the above mentioned model could only be applied above 4.2K and at 4.2K, the electrical resistivity rapidly fell to non measurable values (figure 2.1). This zero electrical resistivity state (values smaller than 10^{-14}) under a specific critical temperature is now called the superconducting state and can be found in a series of other metals and alloys [4].

Later, it was established that superconductive materials are characterized not only by their zero resistivity, but by a whole range of special properties that are observed under a specific critical temperature T_C , critical field $H_C(T)$ and critical current density $J_C(T, H)$.

Other special properties of superconductors:

2.1.1 Meissner-Ochsenfeld Effect

The Meissner-Ochsenfeld effect is the expulsion of the magnetic field from the inside of a superconductive material in its superconducting state. This property however can not be explained just by taking the zero resistivity property into consideration alone. For further illustration of this problem, let us consider an ideal conductor ($\rho (T < T_C) = 0$) and two paths in the HT-diagram in figure 2.2 [5]. Superconducting materials at temperatures and fields below the H_C - T_C curve are in the superconducting state, above it they are in the normal state.

Putting the formulas of Ohms rule, definition of voltage, Stokes theorem and a Maxwell equation, respectively into use, the following formula for an ideal conductor is obtained.

$$0 = IR = U = \oint_C \vec{E} \cdot d\vec{l} = \int_S \text{rot } \vec{E} \cdot d\vec{S} = -\frac{\partial \vec{B}}{\partial t} \cdot \vec{S}$$

This formula states, that the magnetic field of an ideal conductor has to remain constant in time at temperatures below the critical temperature.

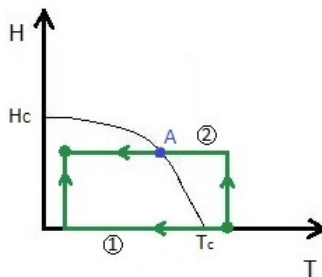


Figure 2.2: HT-diagram and two possible paths, 1 and 2

Following path number one in figure 2.2, the material goes through zero field cooling first and only after achieving temperatures, where resistivity is zero, a magnetic field is applied. This field is expelled from the inside of the material to keep the magnetic field inside constant in time: $B_{int}=0$.

Following path number two brings different results. First the external field is applied and then the material is cooled down. In this case to keep the magnetic field constant in time inside the material, the inner magnetic field has to be equal to the outside field even below the critical temperature: $B_{int}=B_{out}$.

Assuming the superconducting state has zero resistivity without any further changes in its properties compared to the normal state, leads to an inequality in B_{int} and a non thermodynamical state. The solution is an additional property of the superconducting state, the Meissner-Ochsenfeld effect. This effect causes not only the inner magnetic field to be unchanged in time, but the inner magnetic field to be zero itself.

Considering that $B_{int} = 0 = \mu_0(H_{out} + M)$, the magnetization is equal to the negative of the applied field, meaning that superconductors behave as perfect diamagnets with magnetic susceptibility $\chi = -1$.¹ In path 2, the outside magnetic field is compensated through Meissner shielding currents flowing at the surface, which come in play in point A and create a field just outside the surface equal to H_{int} . The expulsion of the field takes place until the applied field reaches a critical magnetic field $H_C(T)$.² Above the critical field, the material switches to the normal conducting state, because at $H_C(T)$ the lower ground state energy of the superconducting state is compensated through the energy needed for shielding currents.

The Meissner-Ochsenfeld effect is explained by the London equations, based on the assumption that the shielding currents occur on the surface reaching only a specific depth λ_L , the London penetration depth. The second London equation explains the occurrence of the superconducting current j_s even in a static magnetic field:

$$\nabla \times (\Lambda \vec{j}_s) = -B \quad \text{with London parameter } \Lambda = \frac{m}{n_s e^2} \quad (2.1)$$

2.1.2 Quantization of the magnetic flux inside a superconductive ring

An even better insight into the behavior of the currents in a superconductor is given by the Ginzburg-Landau equations, based on the Landau theory for second order phase transitions. The Landau theory describes the development of a parameter n_S , that is finite for $T < T_C$, but equals zero at $T > T_C$. The chosen parameter n_S for the Ginzburg-Landau equations

¹These conclusions only apply, if $H_{int} = H_{out}$. The inner field of a sample is defined as $H_{int} = H_{out} - H_D$, where H_D is the demagnetization field and is equal to $D * M$, with the geometry dependent demagnetization factor D . The demagnetization factor D can have values between 0 and 1. If $D=0$ the above described behavior takes place.

Otherwise applies $B_{int} = 0 = \mu_0(H_{int} + M) = \mu_0(H_{out} + M(1-D)) \rightarrow M = -H_{out}/(1-D) \rightarrow \chi = -1/(1-D)$
²In case of a non zero demagnetization field after an applied field reaches $H_C(T)*(1-D)$, a switch to a normal conducting state should occur, because $H_{int} = H_C(T)$. If this would in fact happen, in normal state $M=0$ and thus $H_{int} = H_{out} = H_C(T)*(1-D) < H_C(T)$. This would again imply a switch back to a superconducting state. Instead of an abrupt switch to a normal state an intermediate state is formed for $H_C(T)*(1-D) < H_{out} < H_C(T)$

is the wavefunction of the superconductive state, $\Psi(\vec{r}) = \Psi_0 \exp[i\phi(\vec{r})]$, where $|\Psi_0|^2$ is the Cooper pair density. Cooper pairs are responsible for the superconductive behavior and their role is better explained in the BCS theory of superconductivity.

Taking into consideration the field-shielding-energy and interface-energies between normal and superconductive areas, two Ginzburg-Landau equations can be derived. The second Ginzburg-Landau equation is an extension of the second London equation and describes the superconducting current. It can be written as an equation for the change of phase:

$$\nabla\phi = \frac{1}{\hbar} \left(\frac{m_s}{q_s |\Psi_0|^2} \vec{j}_s(\vec{r}) + q_s \vec{A}(\vec{r}) \right) \quad (2.2)$$

Using this equation to calculate the magnetic flow in a superconductive ring, an interesting phenomenon comes up. First one must calculate the line integral of the equation 2.2 around a closed path within the superconductor, deep enough so that $\vec{j}_s = 0$. After the integration of the left side, the change in phase, has to be equal to an integer multiple of 2π , because the wave function after a full cycle has to be unchanged. After some reordering and an application of the Stokes theorem the final result is obtained:

$$\frac{n \hbar}{q_s} = \int_S \vec{B} \cdot d\vec{S} = \Phi_0 \quad (2.3)$$

The resulting magnetic flow enclosed through the superconductive ring is quantized.

2.1.3 Jump in specific heat C

For a proper description of the specific heat in superconductors a favorable variable is the Gibbs free energy G. The formula :

$$G_N(0, T) - G_S(0, T) = \frac{V B_C^2}{2 \mu_0} \quad (2.4)$$

represents the condensation energy lost after the transition to a superconductive state from a normal state. Difference in specific heat (the jump) can be calculated from the second temperature derivation of Gibbs free energy, multiplied with the negative of the temperature:

$$\Delta C = C_S - C_N = \frac{VT}{\mu_0} \left[\left(\frac{\partial B_C}{\partial T} \right)^2 + B_C \left(\frac{\partial^2 B_C}{\partial T^2} \right) \right] \quad (2.5)$$

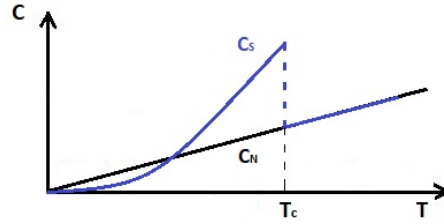


Figure 2.3: Specific heat diagram for normal materials and superconductors

Figure 2.3 displays the differences in specific heat between normal and superconducting materials.

For $T > T_C$: $B_C = 0$ and $\left(\frac{\partial B_C}{\partial T}\right) = 0$. Above the critical temperature $\Delta C = 0$ and both C of superconducting and normal state follow the specific heat represented in the Sommerfeld model, where C grows linearly with temperature: $C_N = \gamma T$, where γ is the electronic specific heat coefficient.

For $T = T_C$: Equation changes to Rutgers formula :

$$\Delta C_{T_C} = \frac{VT_C}{\mu_0} \left(\frac{\partial B_C}{\partial T} \right)_{T_C}^2. \quad (2.6)$$

Rutgers formula gives the value for the jump in specific heat and confirms a second order phase transition at T_C .

For $T \rightarrow 0$: Specific heat of superconductors has an exponential drop, which points to the existence of an energy gap.

2.1.4 Energy gap

As previously mentioned the superconducting behavior can be explained by the BCS theory. The BCS theory extends the calculation of the Cooper problem. The Cooper problem solves the Schrödinger equation for 2 electrons outside the Fermi level ($k_1, k_2 > k_F$) in the presence of an attractive potential V between the two electrons. As a result it is found that the 2 electrons forming a bound state have an energy below $2E_F$. From this it can be concluded that it is energetically favorable to couple the electrons above Fermi sea, making the original ground state unstable. These 2 coupled electrons have opposite spin and impulse and are referred to as the Cooper pair.

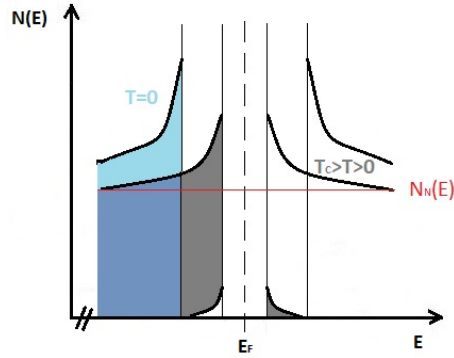


Figure 2.4: The single particle (Quasiparticle) representation of the density of states. Paired electrons are pushed out of the gap region causing peaks on the edges of the gap

The electrons are coupled through lattice vibrations (phonon interactions). As an electron moves through a lattice of ions, the ions are being attracted towards it and creating a positive cloud. Since the mass of ions is much larger than that of electrons, this cloud remains on the spot even after the electron moves away. The positive cloud attracts another electron towards it (with opposite impulse), linking the movement of the second electron to the first one. They can couple over a 100 nm range (lattice spacing is only 0,1 nm).

Paired electrons condense to the same energy level similarly to Boson like states, creating a very small gap (in meV range) around the Fermi level in the single particle representation of the density of states. This gap protects the state from being destroyed and prevents scattering, that otherwise causes resistance. The gap is largest at $T=0K$ and decreases, because the binding energy is weakening with temperature, until T_C , where the gap vanishes completely (figure 2.4).

All particles in the superconducting state condense to the same energy level and can be described with a collective wavefunction [6].

2.1.5 Isotope effect

The critical temperature depends on the number of neutrons in the lattice atoms, which define the mass of the respective isotope. This hints to phonons contributing to superconductivity and confirming the assumption, that Cooper pairs are coupled via lattice vibrations.

2.2 Classification of superconductors

Superconductors are divided into two categories: type I and type II superconductors.

A type I superconductor expels the magnetic field fully up until it reaches a critical field

B_C . At B_C a phase transition from superconducting state to a normal conducting state takes place.

A type II superconductor is defined by two critical fields: a lower critical field B_{C1} and an upper critical field B_{C2} . Below the lower critical field B_{C1} the type II superconductor experiences a full expulsion of the magnetic field from the inside of the superconductor. Crossing of the B_{C1} however causes magnetic flux vortices to penetrate the material. The magnetic flux vortices carry an identical quantum Φ_0 of flux, and are each surrounded by current shells, keeping the rest of the material superconducting. They are arranged in a special triangular shaped lattice with the lattice spacing d being $(1.15\Phi_0/B)^{0.5}$. Only after crossing B_{C2} a transition to a normal conducting state takes place. The state of the superconductor between the two critical fields is called the Shubnikov state. The question if it is energetically favorable for a material to let in these magnetic flux vortices (new interfaces), is answered based on the value of the Ginzburg - Landau parameter κ :

$$\kappa < \frac{1}{\sqrt{2}} \rightarrow \text{type I. Superconductor}; \quad \kappa > \frac{1}{\sqrt{2}} \rightarrow \text{type II. Superconductor} \quad (2.7)$$

The Ginzburg - Landau parameter κ is the ratio between the magnetic penetration depth λ and the coherence length ξ . Whilst λ is the distance from the surface required for the outside magnetic field to fall to 1/e of its original value inside the superconductor and depends on the superconducting electron density, ξ is linked to the transition length between a normal and a superconducting state.³

2.2.1 Critical current density

In section 2.1.1 was stated that superconductors lose their superconducting properties above the T_C - $B_C(T)$ curve. The Silsbee hypothesis further explains the existence of a critical current density J_C for type I superconductors. A current flowing in a superconducting sample creates a magnetic field B_I . This field is accumulated just outside the surface of the superconductor and added to the expelled magnetic field B_{int} . If the current is being increased, eventually the magnetic field at the surface, $B_I + B_{int}$, will exceed $B_C(T)$ and the sample will change to its normal state. The current density resulting in $B_C(T)$ at the surface is the critical current density $J_C(T,B)$.

³In the BCS theory exclusively ξ is the size of the Cooper-pair

The critical current density J_C for the type II superconductor can be explained as follows. After the magnetic field on the surface exceeds B_{C1} , magnetic flux vortices penetrate the sample. Lorentz force is being applied to the magnetic flux vortices as a consequence of the currents flowing through the sample ($J=dq/dV \cdot v$) interacting with the magnetic field vortices ($B=n\phi_0/A$) and is defined as $dF_L/dV= J \times B$. The opposing force that is trying to anchor the vortices to pinning centers in the lattice, is the pinning force F_P . As long as F_L is smaller than F_P , the vortices are pinned to the pinning centers. Only after F_L is larger than F_P , the vortices loosen from their position and start to move through the sample. Moving vortices cause a flux flow resistivity. The critical current density J_C is now described as the maximum current density allowed before the vortices start to move and the resistivity starts to raise from zero. All of this is summarized in the equation: $F_P=F_L=J_C \times B$.

Critical current density can be raised by generating defects in the crystal structure that act as point pinning centers and pin the vortices even at higher Lorentz forces. The pinning is due to the different superconducting nature between the defect and the matrix, causing a difference in free energy and thus creating an attractive force F_P of the defect on the flux vortices [7].

2.3 Nb₃Sn

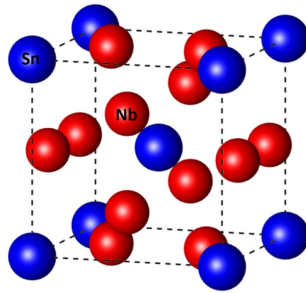


Figure 2.5: A15 compound unit cell structure [8]

The intermetallic material Nb₃Sn is an A15 phase superconductor of type II. All A15 compounds have the stoichiometry A₃B, in this case A being Niobium and B being Tin, as well as a specific structure pictured in figure 2.5. The superconducting phase Nb-Sn occurs anywhere between 18 to 25 at.% Sn, but will in general be described just with Nb₃Sn for any Sn content between these values.

A15 compounds are superconductors many of which have a relatively high critical temperature and remain superconductive in high magnetic fields. This would also be the case

of Nb_3Sn . All of the main properties are summarized in table 1. It must be stated, that the superconducting properties are strongly dependent on the exact compositions of individual samples and the tabulated values are only given to serve as guidance. They are the values for 25 at.% Sn on Nb_3Sn wires. Plots of the development of these values with Sn content are available in Appendix A.

As previously mentioned in the introduction, the superconducting material is very brittle and requires special manufacturing methods to construct wires. The most widely used method is the bronze technique. In this technique, Nb rods are inserted into a Cu(Sn) bronze alloy and shaped into wires. Only after the final shape is achieved, reaction heat treatment will start. Temperatures between 600 to 800°C will start a diffusion process, creating Nb_3Sn on the interface of Nb/Cu(Sn). The cross section of a filament produced in this way can be found in figure 2.6. Studies of the growth mechanism of Nb_3Sn created using this method showed that Sn is the faster diffusing atom through the product phase [9].

T_C [K]	$B_{C2}(0K)$ [T]	$\lambda(0)$ [nm]	a_0 [Å]
18.2	24.5	≈ 100	5.289

Table 1: Some of Nb_3Sn properties for 25 at.% Sn measured Nb_3Sn wires[10, 11]

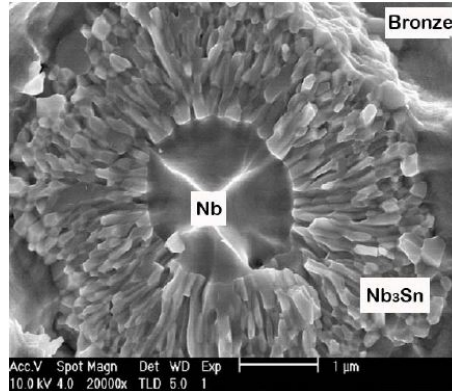


Figure 2.6: Growth of Nb_3Sn at the Nb/Cu(Sn) interface [9]

3 Radiation induced and annealing effects on A15 superconductors

Irradiating the A15 superconductors with neutrons, electrons, protons, deuterons, α particles or heavy ions, all introduce disorder in the form of a defect into the lattice. These defects then cause changes in the superconducting properties. A collision of the radiation particle with the sample lattice can for instance create Frenkel defects, vacancies or antisite defects.

The following subsections conclude of an overview of all the measured superconducting parameters, completed with theory and a literature review of previously measured changes. This knowledge is used for later data interpretation. The methods with which these parameters were obtained are described in section 4 Experimental methods.

3.1 Lattice parameter, long range order parameter and mean displacement amplitude

The lattice parameter a_0 , size of the unit cell, was observed to increase with radiation. Sweedler et al. [12] suggested that this expansion of lattice could be caused by anti-site defects. Larger Nb atoms, with radius of 1.51\AA , occupy the position of the smaller Sn atoms, with radius of 1.41\AA . However independent experiments by Nölscher and Flükiger [13, 14] both showed that irradiating Nb_3Sn and Nb_3Ge with the same dosage resulted in the same a_0 expansion, which is in conflict with Sweedlers theory. According to Sweedlers theory a substitution of the Ge atom, with the radius of 1.35\AA , should result in a larger a_0 expansion than the expansion created by substitution of the larger Sn atom. Nölscher and Flükiger ascribed the expansion to decreasing covalent bonding in the Nb chains.

The long range order (LRO) parameter S is a descriptive value of the lattice periodicity and regularity. A completely ordered lattice is assigned to S equal to one. S decrease is from the definition of S caused by antisite defects (A site occupied by B atom or vice versa). X-ray measurements by Flükiger and Sweedler on irradiated samples show a change in S dependent on the radiation fluence n [12, 15]. It was Aronin [16] that developed an equation to describe their mutual relationship. This equation is as follows:

$$S = S_0 e^{-kn} \quad , \quad (3.1)$$

where S is the value after irradiation and S_0 is the unirradiated sample value. S_0 is set to be equal to 1. k is the proportionality constant, that is dependent on material as well as the radiation beam energy and can be interpreted as the number of replacements per primary knock-on. In the case of Nb_3Sn Sweedler [17] assumed the value of k is going to be the same for Nb as well as for Sn. This statement is justified by their similar elastic cross section and mass.

Exact values for k have to be found via a fit on X-ray measurements of S . For Nb_3Sn Sweedler reported a $k = (0.9 \pm 0.3) \cdot 10^{-20} \text{ cm}^2/\text{n}$ [17], Shiota reported a $k = 2.2 \cdot 10^{-20} \text{ cm}^2/\text{n}$ [18] and Brown a $k = 1.3 \cdot 10^{-20} \text{ cm}^2/\text{n}$ [19].

Mean displacement amplitude $\langle u^2 \rangle$ describes the displacement of an atom from its regular position. An increase in $\langle u^2 \rangle$ is caused by Frenkel defects. An increase in $\langle u^2 \rangle$ with radiation dose was recorded by Meyer et al. on Nb_3Ge and on Nb_3Sn by Burbank et al. [20, 21].

3.2 Critical temperature

Through experiments it was observed that the critical temperature is being reduced through irradiation [12, 22, 23]. The relationships between decrease of T_C and the radiation fluence n is the main interest of these experiments. T_C for different fluences n is directly obtained by measuring T_C after each individual irradiation step. Experiments showed that below the fluence of 10^{18} n/cm^2 the depression in T_C is relatively small, around 5% decrease from the original value. For a fluence of $5 \cdot 10^{19} \text{ n/cm}^2$ the depression is 84.5% from the original value. In figure 3.1 is displayed the dependence for a number of A15 compounds as measured by Sweedler [12].

A mathematical description of this curve was first given by Bett [24]. The suggested equation represents a linear behavior between T_C changes and n as follows:

$$\frac{T_C}{T_{C0}} = 1 - \beta n \quad ; \quad (3.2)$$

where β is a material specific constant, T_C is a value after irradiation and T_{C0} the unirradiated value.

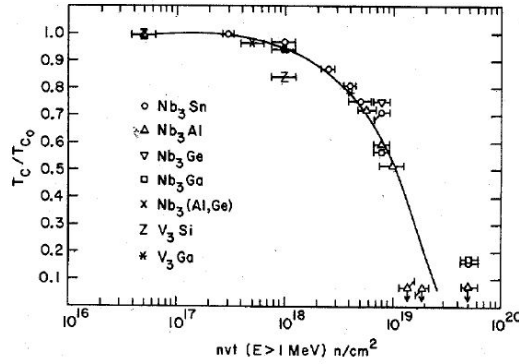


Figure 3.1: Typical curve for T_C in relationship to fluence n [12]

Betts equation was proven unsatisfactory. Hahn [25] later on suggested a new exponential relationship between the two parameters with:

$$\frac{T_C}{T_{C0}} = e^{-\beta n} \quad (3.3)$$

Even this equation did not provide agreement with all experimental data, however the right side of his equation resembles the Aronin equation 3.1. This correctly hints to the fact, that since radiation changes are expected to be caused by defects, a mathematical description of this curve should include the long range order parameter S . The following Pande equation [26] was as well evolved around this idea, resulting in:

$$\frac{T_C}{T_{C0}} = e^{-\alpha(1-\frac{S}{S_0})} \quad , \quad (3.4)$$

where α is a constant independent of fluence and can only be found through a fit to the measured curve. Predictions from only two T_C values about the development of T_C are possible. Shiota [18] found that only two measurements at $n=0$ and n at the order of 10^{18} n/cm^2 , result in an α from the Pande equation 3.4 that can with sufficient accuracy describe the full fluence range. For Nb_3Sn α is found to be around 5 ± 1.5 [17].

S/S_0 in the Pande equation is either directly measured through X-ray or replaced by the Aronin equation 3.1, resulting in a two parameter (k and α) fit of the curve.

For very low fluences Betts, Hahns and the Pande equation coincide, as can be quickly proven by a simple Taylor expansion of the exponential functions. It follows that $\beta = \alpha * k$. This means that for low fluences we can approximate by a linear behaviour between T_C and n (from eq. 3.2), but also by $\frac{T_C}{T_{C0}} = \left(\frac{S}{S_0}\right)^\alpha$ (from eq. 3.3).

The description of the form of the T_C curve with the Pande equation agrees very well with measurements. Pande equation describes change of T_C with change in S , and since S changes with the presence of antisite defects, it is stated that the T_C change through irradiation is caused by antisite defects as well.

A description of the form of the curve from a different perspective is provided in the paper written by Karkin et al. [22]. Besides measuring the change in T_C with n , they also measured the change in transition width ΔT . This is the width in the temperature region from when the superconducting state starts to change, until it completely disappears. What they observed was a bell shaped curve. This suggests the existence of microregions, where T_C is different from the matrix. Karkin explains that the mechanism of disordering can be explained via the theory of displacement spikes. A knocked out atom through radiation travels through the lattice until a point, where its energy is transferred to the lattice and creates a local melting point. Since the time of cooling down is only 10^{-12} s [27] a completely disordered microregion is fixed. This microregion has a much lower T_C than the matrix surrounding it. The higher is the dose, the more of disordered microregions there are. Karkin assumes that until the distance between the individual microregions reaches the coherence length (3.5 nm for Nb_3Sn), the change in T_C is very small. At the fluence $n = 10^{18}$ n/cm² the distances decrease to the coherence length and according to the proximity effect can now influence each other, as well as the surrounding matrix, causing the T_C value to be heavily influenced by the properties of the microregions.

Experiments performed on differently damaged samples of Nb_3Pt (neutron irradiated [28] and fast quenched [29]), introducing different defects into the lattice, resulted in correlation between the long range order parameter S and T_C (same T_C values at the same S values for all samples). Since S changes with the anti-site defect amount, it confirms that the anti-site defects play an important role in the T_C change.

The possibility of T_C changes being caused by Frenkel defects was also investigated. Flükigers experiments showed the same value of T_C at different displacements $\langle u^2 \rangle$ [14]. Since $\langle u^2 \rangle$ changes with the amount of Frenkel defects, this theory was eliminated. Schneider et al. showed no trace of displacement in Nb_3Al films irradiated with low fluences at which T_C change was already recorded [30]. Nölscher showed on a Nb_3Sn sample that annealing of the previously irradiated sample recovered $\langle u^2 \rangle$ in the first anneal step at a very low temperature, whilst T_C stayed unchanged [13]. These are further confirmations that Frenkel

defects are most probably not responsible for T_C degradation.

Annealing experiments on previously irradiated Nb_3Sn samples resulted in a full recovery of the critical temperature T_C [12, 22]. The experiments can either be isochronal, steps with increasing temperature but constant time interval, or isothermal, steps with constant temperature but increasing time interval. Each of these approaches lead to different interpretations of T_C data. Since the used method in this thesis was the isochronal annealing, in the next section only the interpretation of isochronally obtained data is going to be discussed to gain information about activation energies.

3.2.1 Reordering kinetics of disordered A15 compounds

The following method was introduced by Dew-Hughes [31]. To interpret the obtained data from isochronal annealing, one must look into the theory of reordering applied on a specific model created for A15 compounds (A_3B) damaged by irradiation. The applied model makes 2 main assumptions: the only relevant defects are anti-site disorders and single vacancies; and reordering is executed by displaced atoms hopping into their original sub-lattice with the assistance of vacancies. The model consists of six possible atom movements and two possible vacancy formations, all of which are described by a corresponding activation energy. The activation energies are:

(1.) $U_{M(A)}$: A atom from A-site to A-site vacancy	}	Self-diffusion/migration energies
(2.) $U_{M(B)}$: B atom from B-site to B-site vacancy		
(3.) $U_{R(A)}$: A atom from B-site to A-site vacancy	}	Reordering energies
(4.) $U_{R(B)}$: B atom from A-site to B-site vacancy		
(5.) $U_{D(A)}$: A atom from A-site to B-site vacancy	}	Disordering energies
(6.) $U_{D(B)}$: B atom from B-site to A-site vacancy		
(7.) $U_{v(A)}$: formation of A-site vacancy	}	Vacancy formation energies
(8.) $U_{v(B)}$: formation of B-site vacancy		
* Migration of an A(B) atom from B(A)-site to B(A) vacancy is very unlikely		

The self-diffusion process can either take place after reaching U_M alone, if vacancies are present from previous radiation, otherwise only after $U_M + U_v$ energies are reached and thermal equilibrium vacancies are formed to assist with hopping. Same goes for the reordering

and disordering processes, either only the energy U_R (U_D) is needed, or $U_R + U_v$ ($U_D + U_v$). Based on these energies and assumptions, Welch developed an equation for the rate of reordering. The rate of reordering is represented by a time development of the parameter ζ . Parameter ζ is equal to $(1-S)$, where S is the long range order parameter. The equation is as follows:

$$\frac{\delta\zeta}{\delta t} = -f_v \cdot \zeta^2 \cdot \frac{12 \cdot \nu_A \cdot e^{-\frac{U_R(A)}{k \cdot T}} \cdot \nu_B \cdot e^{-\frac{U_R(B)}{k \cdot T}}}{\nu_B \cdot e^{-\frac{U_R(B)}{k \cdot T}} + \frac{3}{4} \cdot \zeta \cdot \nu_A \cdot e^{-\frac{U_R(A)}{k \cdot T}}} , \quad (3.5)$$

where f_v is the amount of vacancies and ν is the frequency of hopping. In section 2.3 it was mentioned, that Sn is the faster diffusing atom through the product phase. This suggests that $[U_M(A) + U_v(A)] > [U_M(B) + U_v(B)]$. Assuming that Sn is more mobile than Nb in the reordering processes as well, leads to $U_R(A) > U_R(B)$ and the equation 3.5 can be written for Nb₃Sn as:

$$\frac{\delta\zeta}{\delta t} = -12 \cdot f_v \cdot \zeta^2 \cdot \nu_A \cdot e^{-\frac{U_R(A)}{k \cdot T}} \quad (3.6)$$

The amount of vacancies f_v changes through time according to the type of vacancy. It is important to mention, that in this model the reordering process itself does not effect the amount of vacancies. Vacancies are simply used as a carrier for the reordering process. The processes that however do effect the amount of vacancies can be summed in the following formula:

$$f_v = f_{v0} \cdot e^{-\frac{t}{\tau}} + f_{ve} \cdot e^{-\frac{U_v}{kT}} , \quad (3.7)$$

where f_{v0} are vacancies created during irradiation and f_{ve} are vacancies present at thermal equilibrium. Radiation created vacancies diffuse to sinks, where they annihilate. Radiation vacancies recede as an exponential function of time and the relaxation time of the vacancies diffusing to sinks τ . On the other hand thermal vacancies are created as an exponential function of vacancy formation energy and temperature.

Inserting equation 3.7 into 3.6, integrating this equation through time from zero to t and finally substituting all the parameters to their i -th temperature step of the isochronal anneal value leads to:

$$\frac{1}{\zeta_i} - \frac{1}{\zeta_{i-1}} = 12 \cdot \nu_A \cdot e^{\frac{-U_R(A)}{k \cdot T_{Ai}}} [f_{v0i} \cdot \tau_i (1 - e^{\frac{-\Delta}{\tau_i}}) + f_{ve} e^{\frac{-U_v}{k T_{Ai}}} \cdot \Delta] , \quad (3.8)$$

where Δ is the time interval of the isochronal anneal and T_{Ai} is the annealing temperature at the i -th step. Plotting $\ln(1/\zeta_i - 1/\zeta_{i-1})$ against $1/T_{Ai}$ can now provide information about the activation energies based on the slope of the resulting curves. The three possible plots are shown in figure 3.2.

Depending on the relationship between the anneal time interval Δ and the relaxation time τ , two special cases of the equation 3.8 are recognized:

- $\Delta \ll \tau$: The slope in the plotted equation is equal to $\frac{-U_R(A)}{k}$
- $\Delta \gg \tau$: The slope in the plotted equation is equal to $\frac{-(U_R(A)+U_v)}{k}$

The relaxation time is depended on temperature in the following way:

$$\tau = \frac{1}{D_0 \cdot e^{\frac{-U_M}{kT}}} , \quad (3.9)$$

where D_0 is a constant. This means that at higher temperatures τ is smaller than at lower, and on a $1/T_{Ai}$ plot the first case will be to the right and second to the left of the curve.

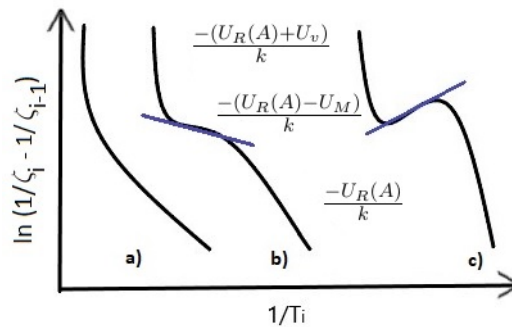


Figure 3.2: Possible plots of the equation 3.8. Blue line representing the middle slope.

An example of this behaviour is curve a) in figure 3.2, that consists of two slopes each representing a different activation energy. The slope to the right, low temperature stage, is equal to $\frac{-U_R(A)}{k}$ and slope to the left, high temperature stage, is equal to $\frac{-(U_R(A)+U_v)}{k}$.

However a third slope between these two may come up as in the case of curves b) and

c). This behavior is typical for materials, where the amount of radiation created vacancies is larger than thermal equilibrium vacancies even at higher temperatures. This is a consequence of U_v being much larger than U_M . In this case the exponential function of U_M in τ is non-negligible for intermediate temperatures. The slope in the middle part is equal to $\frac{-(U_R(A)-U_M)}{k}$. Curve b) represents the case, when $U_R(A) > U_M$, whilst in curve c) $U_R(A) < U_M$, which results in a negative middle slope. Both of these curves are representing a three stage temperature recovery.

As mentioned in section 3.2 T_C/T_{C0} can be approximated to S/S_0 for low fluences. This allows to replace ζ_i through $y_i=1-(T_{Ci}/T_{C0})$ in equation 3.8:

$$\frac{1}{y_i} - \frac{1}{y_{i-1}} = K \cdot e^{\frac{-U_R(A)}{k \cdot T_{Ai}}} [f_{v0i} \cdot \tau_i (1 - e^{\frac{-\Delta}{\tau_i}}) + f_{ve} e^{\frac{-U_v}{k T_{Ai}}} \cdot \Delta] \quad (3.10)$$

The activation energies can now be calculated using only isochronal annealing data, T_{Ci} vs. T_{Ai} .

3.3 Upper critical field

Dependence of B_{c2} on fluence n is represented by a complex curve and can be explained based on the principles of the GLAG theory [32]. The expression for B_{c2} , with Ginzburg-Landau parameter $\kappa (= \lambda_L/\xi_0)$, at the vicinity of T_C is:

$$B_{c2} = \kappa \sqrt{2} B_c \quad (3.11)$$

To correctly define the development of κ during irradiation, and therewith B_{c2} , we must first consider the purity of the sample. Introducing impurities into the lattice will cause scattering of the electrons on the defects. The length between collisions is called the electron mean free path l . As is described in the GLAG theory, comparing l with the coherence length ξ_0 (equal to the size of the Cooper pair as defined in BCS) divides superconductors into two limits:

$$l \gg \xi_0 \rightarrow \text{clean limit and } l \ll \xi_0 \rightarrow \text{dirty limit}$$

In the dirty limit the scattering on defects has to be taken into consideration. The values of ξ_0 and λ_L from the clean limit are replaced by the so called effective ξ and λ , these are now dependent on the electron mean free path l : $\xi \approx \sqrt{\xi_0 l}$ and $\lambda \approx \lambda_L \sqrt{\xi_0/l}$. The effective Ginzburg-Landau parameter is hence: $\kappa \approx \lambda_L/l$. Gor'kov Goodman introduces the

dependencies of λ_L and l ($\gamma^{-3/2}$ and $\gamma^{-2}\rho^{-1}$ respectively [10, 33]), and creates an equation for the dirty limit that calculates the change in κ with impurities:

$$\kappa = \kappa_0 + C_1 \sqrt{\gamma} \rho, \quad (3.12)$$

where κ_0 is the value for κ before irradiation, γ is the linear electronic specific heat coefficient (Sommerfeld coefficient), ρ is the normal state resistivity and C_1 is a constant. Normal state resistivity based on the Drude model can be written as:

$$\rho = \frac{m * v}{e^2 * n_e * l}, \quad (3.13)$$

where m , v , e and n_e are the mass, velocity, charge and charge density for an electron. GLAG theory also defines the B_C field from equation 3.11 with a constant C_2 as follows:

$$B_C = C_2 * T_C \left(1 - \frac{T}{T_C}\right) \sqrt{\gamma} \quad (3.14)$$

Setting equations 3.12 and 3.14 into 3.11 provides an equation for the upper critical field in the dirty limit as defined by the GLAG theory:

$$B_{C2}(dirty) = C_3 * T_C \left(1 - \frac{T}{T_C}\right) \gamma \rho \quad (3.15)$$

Introducing defects into the lattice will cause l to decrease, hence increase ρ , κ and ultimately B_{C2} . This however will be the case only for low fluences, where T_C -change is very small. At higher fluences, where T_C experiences a very steep decrease, the B_{C2} increase caused by ρ increase will be compensated by a decrease in B_C . At higher fluences B_{C2} will decrease. This behavior is captured in figure 3.3 based on Meier-Hirmer et al. measurements of V_3Si crystals [23]. The initial H_{C2} increase, caused by Ginzburg Landau parameter increase, peaks around the irradiation dose 10^{18}cm^{-2} . The irradiation dose 10^{18}cm^{-2} corresponds to the threshold dose for V_3Si from figure 3.1 after which T_C rapidly decreases.

Since B_{C2} is temperature dependent, it is important to note that all of these predictions are only valid in the vicinity of T_C .

3.4 Penetration depth

As discussed in the previous section 3.3 the effective penetration depth λ in the dirty limit based on the GLAG theory is defined as $\lambda \approx \lambda_L \sqrt{\xi_0/l}$. After the introduction of

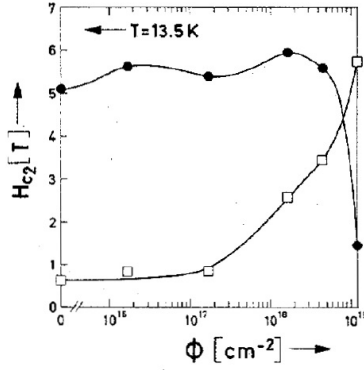


Figure 3.3: Upper critical field and Ginzburg-Landau parameter for V_3Si crystals dependence on the irradiation dose Φ [23]

the dependencies of λ_L , l and ξ_0 ($\gamma^{-3/2}$, $\gamma^{-2}\rho^{-1}$ and γT_C^{-1} respectively [10]), the effective penetration depth in the dirty limit is:

$$\lambda(\text{dirty}) = \sqrt{\frac{\rho}{T_C}} \quad (3.16)$$

Introducing defects into the lattice will cause ρ to increase (eq. 3.13). T_C as described in section 3.2 will decrease with defects. These behaviors combined result in a λ increase with irradiation.

3.5 Critical current density

The shape of the curve representing dependence of the critical current density J_C on fluence n is similar to the one of B_{C2} , a curve with a peak. It raises up until a certain amount of fluence and then starts to decrease. Based on the definition of J_C (section 2.2) a correlation between B_{C2} and J_C is obvious. The occurrence of the point, where the parameters start to decrease, at approximately the same fluence for both B_{C2} and J_C supported the idea of Parkin and Snead that the J_C behavior is mainly influenced by B_{C2} changes [34]. However later studies by Küpfer et al. revealed that the main influence might actually be the number of defects created in the sample, giving raise to a pinning force, especially for the behavior around the peak (low fluences) [35, 36].

Brown et al. [37] did a research, where J_C/J_{C0} was plotted against fluence, where J_{C0} is the critical current of the unirradiated sample. The critical current density was measured always at the same temperature, but at different applied magnetic fields B . These measurements resulted in J_C/J_{C0} values being higher for higher applied magnetic fields, with the

difference most obvious in the point of the peak. This high sensitivity of J_C/J_{C0} to the applied magnetic field is a demonstration of the pinning force having a big contribution in the behaviour of J_C with fluence.

To summarize, the initial J_C increase with fluence is due to increased number of pinning centers and increase in B_{C2} , whilst saturation and decrease of J_C is due to saturation in pinning and decrease of B_{C2} .

4 Experimental methods

The following sections describe the experiment execution and the methods with which the structural and superconducting parameters were obtained from raw data.

4.1 Sample preparation and description

Samples used in this thesis were two bulk Nb₃Sn plates provided by Tiziana Spina and René Flükiger from CERN. The samples were prepared using the HIP (Hot Isostatic Pressure) process, that is used to reduce the porosity of the processed materials. They were created from a mixture of Nb and Sn powders, with a mass ratio chosen to give raise to a 24.8 at. % composition. As can be seen on the Nb₃Sn phase diagrams, the composition rate was deliberately chosen lower than 25 at. % to lower the risk of creating the two phase Nb₃Sn + Nb₆Sn₅ regions. The HIP treatment subjects the mixed powder to an elevated temperature and gas pressure from all directions (hence isostatic) inside a vessel. The samples were HIP treated at the temperature of 1250° C at 2 kbar Argon pressure. The created Nb₃Sn block was next cut to two thin plates by spark erosion and finally polished to the dimensions 2.5×2.5×0.6 mm. An exact description of this process can be found in the work of Tiziana Spina [41].

From the two plate samples, one sample was being studied in its bulk form, the other sample was pulverized. The pulverized sample was mixed with a silicon standard powder, to be used as a scale for the X-ray measurements, and enclosed in a quartz tube in vacuum. Both samples are displayed in figure 4.1.

The effect of neutron radiation on T_C , B_{C2} and J_C was studied on the bulk sample and afterwards the effect of post-radiation annealing on the same set of parameters. The pulverized sample was specifically used for x-ray measurements, to gain information about the lattice parameter and its change with the post-radiation annealing. The pulverized sample was also used for a study of the penetration depth λ , that can not be performed on bulk samples. B_{C2} and J_C measurements were not performed on the pulverized sample, since high magnetic fields, fundamental for these measurements, cause movement in the fine powder, and thus inaccuracy in the data.

The bulk sample cracked into multiple pieces during the annealing process at 500°C. After this crack occurred, the sample was cleared of all lose pieces and used for the following

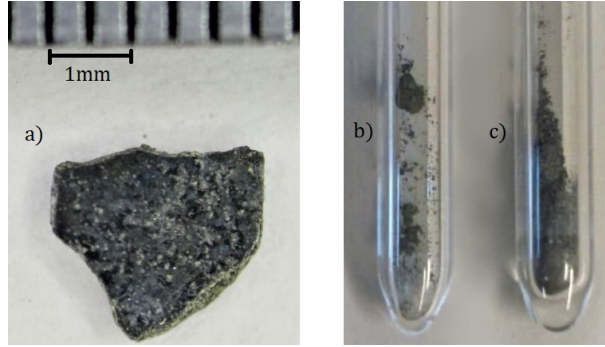


Figure 4.1: Nb₃Sn samples: a) bulk sample after 500°C anneal with visible oxidation and changed geometry from original square of 2.5×2.5 mm ; b) bulk sample after 550°C anneal enclosed in vacuum with a larger piece in the upper part of the quartz tube; c) powder sample with Si standard under vacuum in quartz tube

measurement and for the next annealing step at 550°C (figure 4.1 a)), however this led to more cracking. The sample had to be enclosed into a quartz tube in vacuum, similarly as the powder sample. The bulk sample now consisted of one larger piece and multiple smaller pieces (figure 4.1 b)). This made the measurement of the effect of annealing on J_C impossible, since the exact sample dimensions are needed for the J_C calculation.

The cracking is suspected to be due to oxidation of the sample. Oxidation was visually seen on the samples surface, as well as in the X-ray measurements on the powdered sample, leading up to 4.9% Niobium Oxide after the 750°C anneal and 9.5% after the 850°C anneal. Further cracking did not occur after the sample was enclosed in vacuum.

For the penetration depth calculation the exact grain size distribution for the powder sample was required. This was done through direct measurements of the powder on a scanning electron micrograph (SEM). The SEM device used was the FEI Quanta 250 FEG at the USTEM department of TU Wien operated with the help of Dipl.-Ing. Stephan Pfeiffer. An example of the obtained image is shown in figure 4.2.

The image processing program ImageJ was used to analyse the grain radii of Nb₃Sn from multiple obtained images. The resulting histogram (figure 4.2) has a peak at radius $r=1.24\mu\text{m}$ and a tail reaching $r=70.55\mu\text{m}$. It was unsuccessfully fitted to Log-normal and Weibull distributions that are known to be good representations of the particle size distributions. The fitted distributions were not capable of correctly simulating the exact shape of the measured histogram, neither predict the long tail of the histogram. This might be a result of an uneven grinding process. As a result of this observation actual measured count of individual radii was used for penetration depth calculations, rather than a fitted distribution.

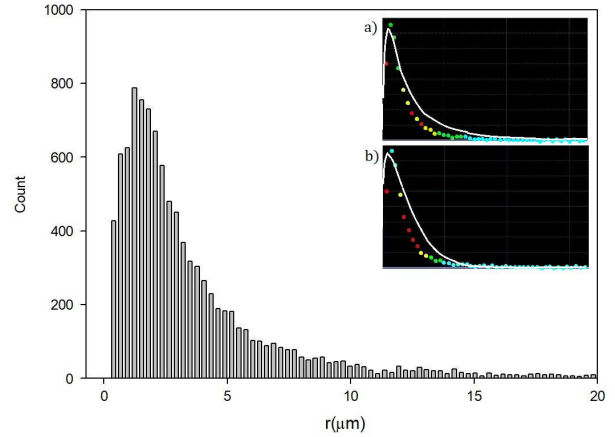
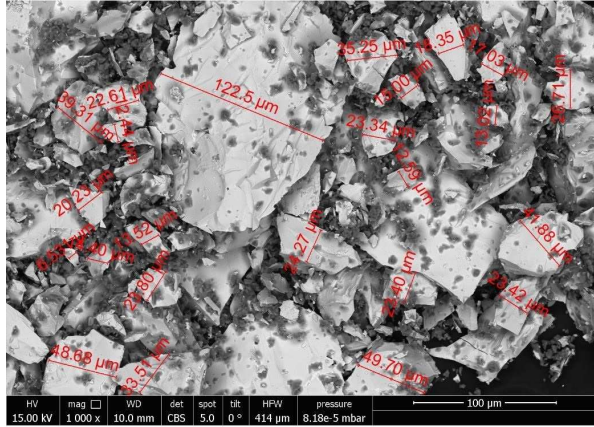


Figure 4.2: SEM image of the powder sample. The lighter grey grains are Nb_3Sn grains, whilst the darker grains are Si grains. On the right is the resulting histogram of the radius r . The long tail of the histogram reaching the radius $70.55 \mu\text{m}$ is not shown. Two fits of the histogram are also included. The solid line is representing in a) the Log-normal distribution and in b) the Weibull distribution

4.2 Irradiation and annealing process

The samples inside quartz tubes were placed in aluminum irradiation capsules and irradiated in the TRIGA Mark-II reactor at the Atominstitut Wien pictured in figure 4.3 a). The samples were irradiated with high energy ($E > 0.1 \text{ MeV}$) neutrons. Both samples were irradiated multiple times with measurements of superconducting properties in between irradiation steps. The final fluence (neutrons per unit area) for either sample after each irradiation step is to be found in table 2 left. The most dominant source of radiation is the ^{113}Sn with a half life of 115 days.

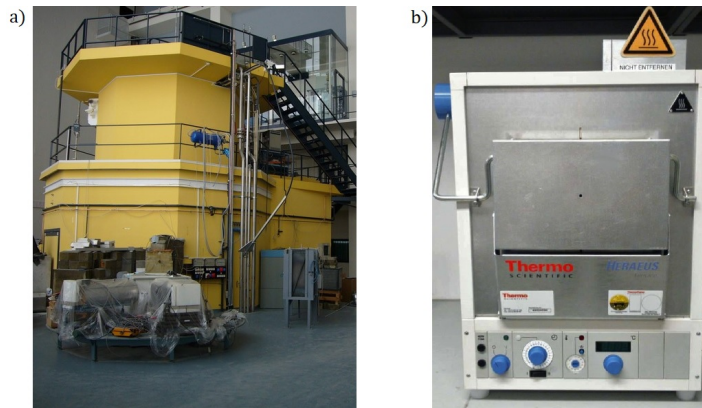


Figure 4.3: Equipment for irradiation and annealing: a) TRIGA Mark-II reactor at the Atominstitut Wien; b) Thermo Scientific Laboratory chamber furnace

Annealing was performed in a chamber furnace from Thermo Scientific pictured in figure

4.3 b). Samples were annealed at annealing temperatures T_A , starting at 300°C temperature all the way up to 900°C with a 50°C step size. The samples were kept at T_A for one hour and afterwards taken out from the furnace to cool down in room temperature. The time for the furnace to reach T_A differed for individual T_A values and a listing of these time periods can be found in table 2 right.

Step	Fluence [n/cm^2]	
	Bulk sample	Powder sample
1.	$9.38 \cdot 10^{15}$	$3.33 \cdot 10^{17}$
2.	$3.93 \cdot 10^{16}$	$8.31 \cdot 10^{17}$
3.	$2.65 \cdot 10^{17}$	—
4.	$6.57 \cdot 10^{17}$	—
5.	$9.38 \cdot 10^{17}$	—
6.	$1.27 \cdot 10^{18}$	—
7.	$1.77 \cdot 10^{18}$	—

T_A [°C]	Time to achieve T_A [min]
300 - 650	80
700 - 750	85
800	90
850 - 900	100

Table 2: Left: Fluence for each irradiation step and sample; Right: Time to achieve annealing temperature T_A for individual annealing temperatures

4.3 X-ray diffraction

After the final irradiation step on the powder sample, the powder sample was divided into three parts. One part was saved in the isotope warehouse of the Atominstitut, another part stayed at the Atominstitut Wien and underwent SQUID measurements after each step of annealing in the furnace, and the last part was carried to the X-ray center Wien. Here XRD-images are obtained using the non-ambient powder diffractometer. These images are further used to calculate structure dependent parameters, for example the lattice parameter a_0 . The results for the silicon standard powder mixed inside the Nb_3Sn powder is used for scale. The measurements were performed by DI Werner Artner using the PANalytical XPert Pro MPD X-ray diffractometer and the results were analysed by Dipl. Dr. Klaudia Hradil.

A non-ambient diffractometer allows the sample to be annealed directly inside the diffractometer. The annealing process performed on the sample in Atominstitut Wien is recreated in the diffractometer with a XRD measurement after each step. This means annealing from 300°C to 900°C with a 50°C step size. During the first attempt of this measurement the XRD measurements were performed after each anneal step at the temperature $T_A-100^\circ C$ instead of waiting for the sample to be always cooled down to the same temperature. This

lead to the resulting lattice parameter undergoing a different lattice expansion after each further anneal step. The lattice change that is only due to post-radiation annealing had to be estimated by subtracting the change in lattice corresponding to thermal expansion. An improved measurement on a not yet annealed irradiated sample saved in the warehouse is in discussion.

4.4 SQUID MPMS

The Quantum design MPMS (Magnetic property measurement system) can detect the magnetic moment of samples to gain information about T_C , B_{C2} , J_C and λ . The main part of the MPMS is a SQUID (superconducting quantum interference device), the source of the instruments remarkable sensitivity to magnetic fields. The high sensitivity enables to measure very small sample sizes which is of big importance working with radioactive samples. More information on the operation of the SQUID can be found in Appendix B. The Quantum design MPMS assembly is described in figure 4.5 [42].

The sample is attached to the sample rod and installed inside the MPMS. Inside the MPMS the sample is surrounded by detection coils and a superconducting solenoid that can produce DC magnetic fields up to 7 Tesla. The SQUID in the MPMS does not directly measure the magnetic field of the sample, instead the sample moves across the detection coils which are connected to the SQUID placed outside of the superconducting solenoid. As the magnetic sample moves through the detection coils, electric current is induced in them and passed with zero loss through superconducting wires towards and through the well shielded SQUID. In this scenario the SQUID functions as a current to voltage converter. Any change in current is captured by a change in voltage, and a change in current is coupled to the magnetic moment of the sample.

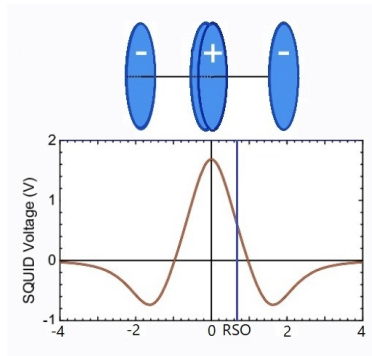


Figure 4.4: Second order gradiometer SQUID response curve [42]

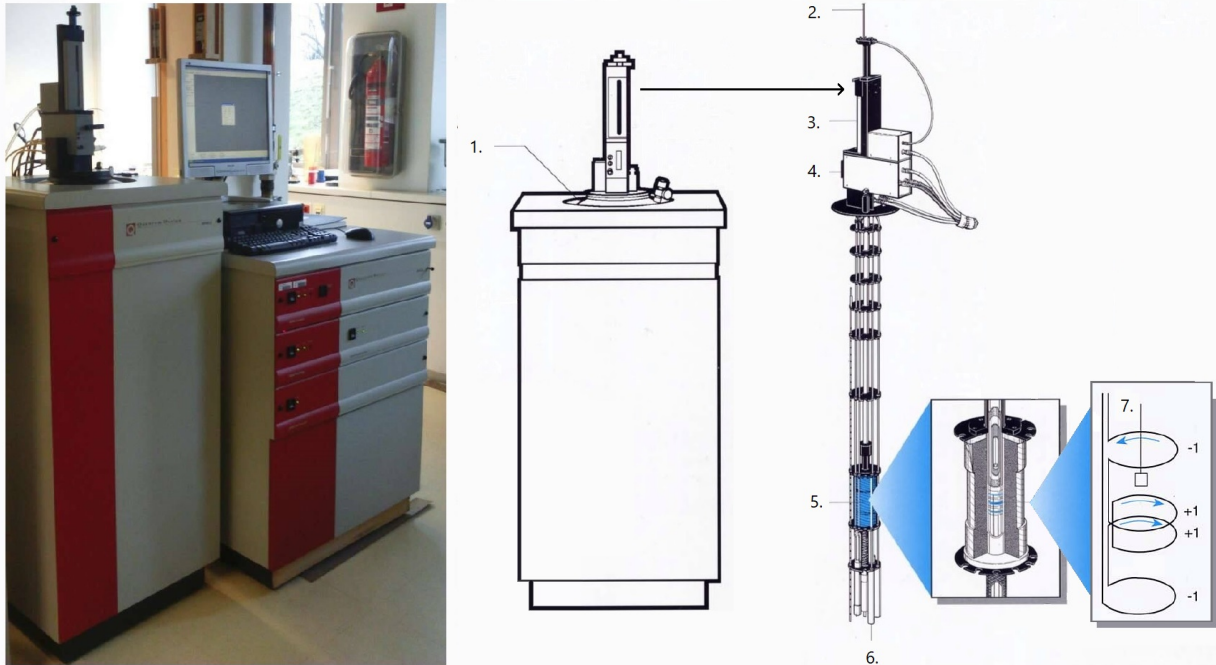


Figure 4.5: Quantum design MPMS XL: 1. Helium cryostat, 2. Sample rod, 3. Standard sample transport, 4. Airlock, 5. Superconducting solenoid, 6. SQUID, 7. Second order gradiometer [42]

The detection coils are three coils configured as a second order gradiometer. Upper coil is a single turn clockwise, followed by the middle coil with two turns anticlockwise, and the bottom coil is a single turn clockwise. The second order gradiometer is used to reduce noise caused by the fluctuations in the outside magnetic field. The voltage is then measured as a function of the position of the sample towards the coils. The final curve is then fitted to a typical second order gradiometer response curve (figure 4.4). The magnitude of this curve is proportional to the magnetic moment. The sample is moved through the coils automatically using the standard sample transport.

Since the superconducting solenoid, the detection coils and the SQUID all require very low temperatures to function, the whole system is placed inside a Helium cryostat and held airtight by purging the sample space before it is inserted into the cryostat.

The MPMS was also used with a RSO (reciprocating sample option) attachment. This attachment can replace the standard sample transport. Whilst the standard sample transport moves the sample in discrete steps through the full length of the detection coils, RSO oscillates the sample using a servo motor over a small region (2 mm) at the most linear part of the second order gradiometer response curve (the maximum slope- figure 4.4). The RSO measurement is fast compared to the standard sample transport measurement, which then allows more averaging and better magnet noise rejection.

Another useful option of the MPMS is to perform measurements using an oscillating AC-magnetic field. A copper coil placed between the detection coils and the superconducting solenoid can produce an alternating magnetic field with a frequency from 0.01 Hz to 1kHz. The measured response of the sample to the AC field is of the form : $m = m'\cos(\omega t) + m''\sin(\omega t)$. m' corresponds to the magnetic moment created through magnetization with the AC field (in literature often referred to as AC susceptibility) and m'' corresponds to the energy dissipation in the sample. The AC measurement of a sample is a two part process. The first part with the sample placed in the bottom coil calculates a nulling waveform to cancel all SQUID responses to AC signals, including the sample signal. The second part of the measurement, with the sample placed in the middle coil, measures a SQUID response and applies the nulling waveform. AC magnetic field signals are removed. Since the sample signal doubles and changes polarity when moved to the middle coil, the now measured signal is the by three-fold enhanced AC magnetic moment of the sample. AC measurements have a high noise rejection and offer high accuracy measurements [43].

The type of MPMS measurement used to collect individual data is presented in the next sections.

4.4.1 Critical Temperature

The critical temperature T_C for both, bulk and powder sample, was obtained through AC measurements with a zero DC field applied. The alternating magnetic field was set to have a 33 Hz frequency and a $30\mu\text{T}$ amplitude. The AC magnetic moment was measured from temperatures below critical temperature upwards. Theoretically at $T=T_C$ the transition to normal state takes place and the magnetization rapidly changes from its initial value to zero. In reality the transition has a specific transition width ΔT and the value for T_C has to be estimated using a favorable method. In the present work T_C was estimated using the 10% method and the onset method. The 10% method determines $T_C^{10\%}$ as the temperature where the AC magnetization m' attains 10% of the m' value at 5K. The difference between temperatures at the 10% value and the 90% value is further determined as the transition width ΔT . The onset method determines T_C^{onset} as the temperature where the AC magnetization m' first crosses the $m'=0$ line. The graphical representation of both methods can be found in figure 4.6. The temperature step during the AC measurement was 0.01K for the bulk sample, and 0.05K for the powder sample at the vicinity of T_C .

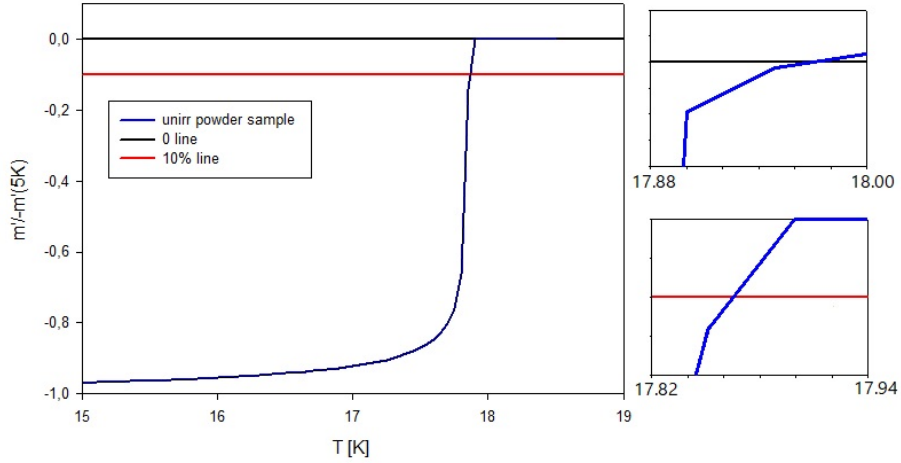


Figure 4.6: AC measurement result for the unirradiated powder sample and a graphical representation of the two T_C estimation methods. The two graphs on the right are close-ups of the individual crossings. The results in this case are $T_C^{onset}=17.9684$ and $T_C^{10\%}=17.8648$.

4.4.2 Upper critical field

The upper critical field $B_{C2}(T)$ was only obtained for the bulk sample. Higher fields applied to powder would cause movement during measurement, which is unacceptable. The $B_{C2}(T)$ of the bulk sample was obtained through AC measurements starting at DC fields above the expected region of $B_{C2}(T)$ and moving on downwards. At $B=B_{C2}(T)$ the transition from normal to superconducting phase takes place and the m' value goes from zero to a specific saturated value. $B_{C2}(T)$ was measured for temperatures from 14.5K to 17.5K with a 0.5K step. During these measurements the alternating magnetic field was set to 10Hz frequency and $395\mu\text{T}$ amplitude.

The results following the cracking of the bulk sample into multiple pieces at 550°C came back with a lot of noise, making it impossible to read out the saturated value for m' . $B_{C2}(T)$ could only be estimated using an onset method henceforth. The onset method determines $B_{C2}^{onset}(T)$ as the magnetic field where the AC magnetization m' first crosses the $m'=0$ line.

B_{C2} is temperature dependent. To obtain results at $T=0\text{K}$, as well as the complete temperature development, one must perform a fit procedure to the measured data at 14.5K to 17.5K. Maki and De Gennes (MDG) derived a microscopic description for the temperature dependence in the dirty limit [44, 45]. The normalized form of MDG relation can be written as:

$$B_{C2}(T) = B_{C2}(0) \left[1 - \left(\frac{T}{T_C} \right)^\alpha \right] \quad (4.1)$$

The power α from recent measurements [46] is calculated to be of the value 1.52. Werthamer, Helfand and Hohenberg (WHH) derived a description for the temperature dependence from the Gor'kov theory taking into account the effects of electron-spin and spin-orbital scattering [47]:

$$B_{C2}(T) = h^*(t) \left(-\frac{dB_{C2}}{dT} \right)_{T=T_C} \cdot T_C \quad , \quad (4.2)$$

where $h^*(t)$ is a function dependent on the paramagnetic limitation parameter α and t is the reduced temperature T/T_C . The paramagnetic limitation parameter α is equal to zero when no paramagnetic limiting is present. Pauli paramagnetic limiting is the depression of the upper critical field as a consequence of the difference between the normal and superconducting magnetic susceptibility. For other values of α , the depression of the upper critical field can be calculated as follows [45]:

$$B_{C2}(\alpha) = \frac{B_{C2}(\alpha = 0) B_P}{\sqrt{2B_{C2}^2(\alpha = 0) + B_P^2}} \quad , \quad (4.3)$$

where B_P is the Pauli limiting field. For Nb_3Sn specifically Orlando et al. [48] calculated the Pauli limiting field to be as big as 94T. Compared to the much smaller upper critical field of Nb_3Sn with values around 24.5T, the equation 4.3 can be reduced to $B_{C2}(\alpha) \approx B_{C2}(\alpha = 0)$ and establishes an absence of the paramagnetic limiting in Nb_3Sn . Without the limiting, $h^*(0)$ was computed to be equal to 0.693 [47]. The zero temperature upper critical field can then be calculated from the WHH relation as follows:

$$B_{C2}(0) = 0.693 \left(-\frac{dB_{C2}}{dT} \right)_{T=T_C} \cdot T_C \quad . \quad (4.4)$$

The WHH relation utilizes the slope of B_{C2} in the vicinity of T_C to calculate its zero temperature value. Substituting the derivative of B_{C2} as defined by the GLAG theory (equation 3.15) into equation 4.4, we obtain : $B_{C2}(0) = 0.693 B_{C2}(T) \left[1 - \frac{T}{T_C} \right]_{T \rightarrow T_C}^{-1}$. The biggest difference between WHH and MDG relation is therefore the power of T/T_C α . At $T/T_C \rightarrow 1$ the caused difference between the two relations on $B_{C2}(0)$ is negligible. The MDG relation is a good first approximation to the WHH theory for Nb_3Sn .

4.4.3 Penetration depth

The penetration depth λ was only obtained for the powder sample, since it is difficult to obtain λ by measurement on large specimen. The used data is the same as was used to estimate T_C , AC measurements with a zero DC field applied, starting at 5K and measuring to 18K.

The magnetic moment is defined as $m=H_0 \cdot \chi \cdot V$, where χ is the magnetic susceptibility and V the volume of the measured sample. Shoenberg formulated an equation for the total magnetic moment of a powder sample by summing over all grains with radius a as follows [49]:

$$m = H_0 \sum_n \chi_{max,n} V_n f(\lambda/a_n) , \quad (4.5)$$

where χ_{max} is the susceptibility value for an ideally diamagnetic grain ($\lambda=0$) and the function $f(\lambda/a_n)$ is equal to χ_{eff}/χ_{max} . The function is calculated by solving the electro magnetic wave function inside and outside of the grain and matching the solutions at the interface. Both χ_{max} and $f(\lambda/a_n)$ depend on the size and shape of the grains. For spherical particles they are

$$\chi_{max} = -3/8\pi \quad \text{and} \quad f(\lambda/a) = \left(1 - \frac{3\lambda}{a} \coth \frac{a}{\lambda} + \frac{3\lambda^2}{a^2} \right) \quad (4.6)$$

After substituting 4.6 into 4.5 and introducing the volume of a sphere, the AC magnetic moment for a powder with spherical shaped grains can be fitted with:

$$m = \sum_n -\frac{H_0 a_n^3}{2} \left(1 - \frac{3\lambda}{a_n} \coth \frac{a_n}{\lambda} + \frac{3\lambda^2}{a_n^2} \right) \quad (4.7)$$

This equation is often averaged over a grain size distribution. In section 4.1 attempts to obtain a satisfactory grain size distribution are shown with negative results, instead summation through individual measured radii multiplied with a variable N is applied.

Shoenberg studied closely the relationship between the AC magnetic moment and the grain shape. He gave solutions of $f(\lambda/a_n)$ for not only spheres, but also for long rods and plates. The limits he found for very small grain sizes and for large grain sizes are summed in table 3.

	Orientation to field H_0	$f(\lambda/a)=f(x)$	
		Large grains	Small grains
Sphere	any	$1-3x$	$1/(15x^2)$
Long rod	\parallel or \perp	$1-2x$	$1/(8x^2)$
Plate	\parallel	$1-x$	$1/(3x^2)$

Table 3: Limits of the f function. x is defined as λ/a . In case of the sphere and long rod a is radius. In case of the plate $2*a$ is the thickness of the plate.

For the sphere the veracity of table 3 can be quickly rechecked by developing the coth in equation 4.6 into a Taylor series. Similar equations to 4.6 leading up to the other mentioned limits can be found for the long rod and plate. From the equations in table 3 we can deduct, that the detailed form of the penetration can best be recovered from measurements on small grains. Whilst a small error in the measurement of m for large grains leads to large errors in λ , for small grains the errors simply correspond to errors in scaling. Scaling errors are errors caused by uncertainties about shape, size and orientation of grains. The best size for the grains is not much larger than the zero temperature penetration depth, but not too small to lose sensitivity. Waldram et al. [50] discovered that for small grain sizes the theoretical result of λ obtained from 4.7, calculated for spheres, agrees well with the result for long rods, if we reduce the radius of spheres by $(15/8)^{1/2}$ and by $(15/3)^{1/2}$ for plates. This procedure was integrated into the final fit of AC magnetic moment to account for the different shapes present in the powder.

The penetration depth is temperature dependent and to gain information about $\lambda(0)$ a proper relation describing the temperature development of λ must be applied.

Daunt et al. suggested a development based on the two-fluid model [51]. In this model the function $W(t)$ describes the number density of superconducting particles divided by the number density of all particles (n_S/n), whilst $1 - W(t)$ describes the number density of normal conducting particles divided by the number density of all particles (n_N/n). In the two fluid model $W(t)$ is equal to $(1-t^4)$.

The penetration depth is defined based on the London's equations as follows:

$$\lambda(T) = \sqrt{\frac{m}{\mu_0 n_S e^2}}. \quad (4.8)$$

Substituting n_S in equation 4.8 with $nW(t)$ and taking into considering that at $T=0$

$n_S = n$, the empirical two-fluid equation can be written as:

$$\lambda(T) = \lambda(0)/(1 - t^4)^{1/2} , \quad (4.9)$$

where t is the reduced temperature T/T_C . Despite the fact that the two-fluid model lacks microscopic description of the superconducting behavior, the equation fits quite well with experimental data, although not perfectly. Since the equation provides a quick useful estimation of $\lambda(T)$, attempts were made to adapt the two fluid equation to results that were calculated using the BCS theory. The fit function had the form :

$$\lambda(T) = \lambda(0)(1 - t^p)^q \quad (4.10)$$

For s-wave superconductors, as is the case of Nb_3Sn , the best fit was achieved with $p=2$ and $q=-0.5$ [52].

However the energy gap is not considered in any of these previous formulas. The energy gap is fundamental for microscopic description and the BCS theory. Bonn et al. suggested a formula that takes the energy gap into consideration with [53]:

$$\lambda(T) = \lambda(0)(1 - t^{3-t})^{-1/2} \quad (4.11)$$

This formulation is the closest approximation to the BCS theory.

4.4.4 Critical current density

The critical current density J_C was obtained for the bulk sample from RSO measurements. The sample oscillated with a frequency of 4Hz over a 2mm region. After the sample broke into pieces at 550°C a switch to DC measurements was made. Two quadrants of a magnetization hysteresis, from 0.1 to 6.5 T and back to 0.1 T, were measured with a 0.1T step, and at two temperatures, 15 and 14K.

The magnetic moment in a hysteresis is called the irreversible magnetic moment m_{irr} and can be calculated through:

$$m_{irr}(H) = \frac{m_{dec}(H) - m_{inc}(H)}{2} \quad (4.12)$$

where m_{dec} is the magnetic moment measured during decreasing applied field and m_{inc} is the magnetic moment measured during increasing applied field.

The relation between J_C and the magnetization hysteresis is based on approximations made in the Bean critical state model [54]. A large hysteresis behavior in the magnetic moment of type II superconductors led Bean to study the theory behind this phenomena. Based on in that time not yet confirmed theory by A.A. Abrikosov, that predicted magnetically quantized vortices to penetrate the sample in type II superconductors, Bean introduced a model of his own, the Bean critical state model. This model similarly to Abrikosov model accepted penetration of the magnetic field, but not in form of vortices. The model assumes that there exists a maximum current density $J_C(H)$ and the shielding current density can only either be equal to $\pm J_C$ or 0.

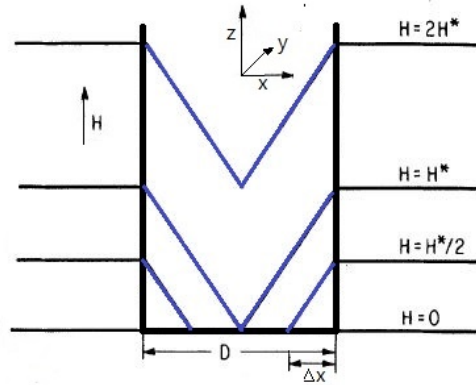


Figure 4.7: Field gradients in a sample of thickness D as a response to different applied fields and their penetration depth Δx [54]

Let us consider a 2D sample in the shape of a rectangle laying in the xz -plane and a magnetic field H in the z -direction (figure 4.7). To shield the sample from the magnetic field a current starts to flow in the y -direction. Based on Amperes law a flowing current density in the y direction will give raise to a field gradient: $\mu_0 J_y = \partial B_z / \partial x$. According to Bean the field gradient has to be constant, because $J_y = J_C = \text{const}$. The depth of the penetration $\Delta x = H / J_C$ grows with H . At the field $H^* = J_C D / 2$ the penetration depth reaches the middle of the sample. For fields $H > H^*$ the sample field can be approximated as $H_{\text{samp}}(x) = H - H^*(1 - 2x/D)$. Considering that there is no demagnetization field, the following equations summarize how to calculate the magnetization M for this particular sample:

$$M = B / \mu_0 - H \quad ; \quad \frac{B}{\mu_0} = \frac{\int_{D/2}^{-D/2} H_{\text{samp}} dx}{\int_{D/2}^{-D/2} dx}$$

$$M = \frac{\int_{D/2}^{-D/2} H^*(1 - 2x/D) dx}{D} = \frac{H^*}{2} = \frac{J_C D}{4} \quad \text{for } H > H^* \quad (4.13)$$

The magnetic moment measured by MPMS is then simply the magnetization M multiplied by the volume V of the sample.

In the present work the used sample is a 3D block. In this case, the correlation of two dimensions, a and b in x and y direction, replace the dimension D . The final equation for the measured magnetic moment is

$$m_{irr}(H) = \frac{J_C(H) b(1 - b/3a)}{4} V \quad \text{for } a > b \text{ and the } ab\text{-plane is perpendicular to } H \quad (4.14)$$

It is important to note that the equation 4.14 is only valid for applied fields higher than H^* . Dimensions of the sample in mm-region ensure the equation 4.14 to be valid already for 10^{-3}T applied magnetic field.

Bean critical state model is able to explain the hysteresis behavior in the magnetic moment, hinting to the models general correctness. Reversal of the applied field causes reversal of J_C starting from the edges of the sample inwards. The condition of a constant field gradient traps the sample magnetic field H_{samp} inside the sample even at $H=0$, and leads to a non zero magnetic moment.

Combining the Bean critical state model and A.A. Abrikosov model leads us to an absolute model. In this model the field gradient predicted in Bean critical state model is created by pinning the vortices on pinning centers starting near the surface. The strength with which the vortices are pinned down is the flux pinning force.

The magnetic hysteresis of type II superconductors may experience the so called flux jumps, where the magnetic moment suddenly drops towards zero (in fig. 4.8 m for $T=14\text{K}$). Flux jumps occur when at specific conditions the magnetic flux abruptly breaks inside the superconductor, causing the superconductors temperature to raise. This causes the critical current density to decrease, allowing even more magnetic flux to enter and increase the temperature. The resulting avalanche process induces the visible flux jump [55].

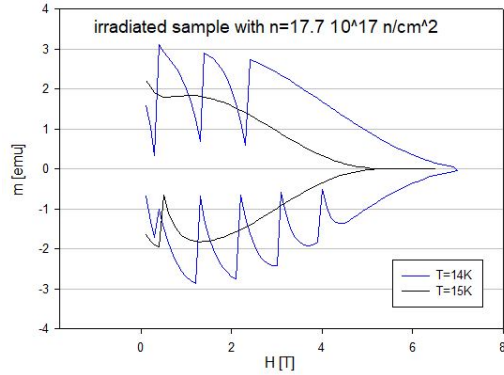


Figure 4.8: Flux jumps occurring in the magnetic hysteresis of a sample irradiated with the fluence $n=17.7 \cdot 10^{17} \text{ n/cm}^2$

The occurrence of flux jumps is depended on temperature, sample size and magnetic field sweep rate. Flux jumps occur more often at lower temperatures, bigger sample sizes and high magnetic field sweep rates. To be able to properly diagnose data from hysteresis measurements using equation 4.14 a suppression of the flux jumps is important.

The shape of the hysteresis for unirradiated samples starts with a certain magnetic moment that is then decreased to zero with applied magnetic field. Defects in the sample influence the shape of this hysteresis. The typical shape of the hysteresis for Nb_3Sn bulk superconductors with defects is the fish-tail shape (in fig. 4.8 m for $T=15\text{K}$). Magnetic moment decreases until a local minimum is reached, starts to increase until a maximum is reached, and afterwards finally decreases to zero. The fishtail shape was correlated to an order-disorder transition of the vortex lattice [56]. At low applied fields the vortex lattice is regular, with the vortices in a triangular shaped mesh. As the applied field is being raised a better adaptation of the vortices on the defect structure is reached, the density of irregular areas in the vortex lattice and the critical current density raise. As the number of defects raises the maximum of the fish-tail is shifted to lower applied magnetic fields [57].

5 Results and discussion

The results obtained from the measurements are discussed in the following sections. The SQUID measurements performed after each irradiation step on the bulk sample were performed by Dipl.Ing. Dr. Thomas Baumgartner prior to the start of this thesis. Gratitude is expressed for the allowance to use this data. Their interpretation and measurements after all annealing steps, as well as all the measurements on the powder sample, were performed by the present author.

5.1 X-ray diffraction

Even after a careful selection of the composition rate to rule out the risk of creating second phase regions, the X-ray measurements showed the existence of a possible second phase with a strongest reflection at $2\Theta = 43^\circ$. As shown in figure 5.1, this peak can either correspond to the intermetallic phase Nb_6Sn_5 or to the NbO oxide [58]. Regions containing one or the other can be considered as additional impurities and will have an influence especially on the flux pinning force.

Caused by the annealing process the amount of NbO in the sample was raised up to 9.5% of the sample mass after the last anneal step.

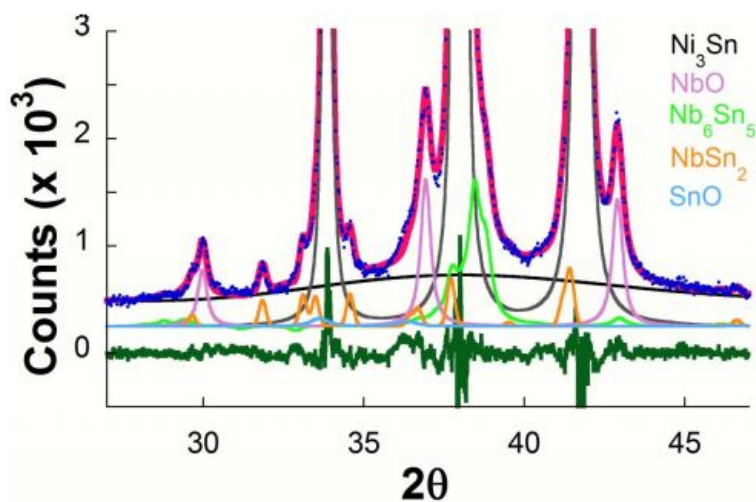


Figure 5.1: XRD pattern for different possible phases and oxides [58]

The lattice parameter a_0 of the unirradiated powder sample was measured to be 5.291882 Å. After irradiation with the fluence of $8.31 \cdot 10^{17} \text{ n/cm}^2$, the lattice parameter raised to 5.292583 Å. This is a 0.013% increase.

The annealing experiments were performed with a methodological error. The XRD measurements were performed after each anneal step at the temperature $T_A-100^\circ\text{C}$ instead of waiting for the sample to be cooled down to the same temperature. This led to the resulting lattice parameter undergoing a different lattice expansion after each further anneal step. The thermal lattice expansion for Nb_3Sn has been calculated using the following expression [59] :

$$\frac{\Delta L}{L(T)} = \frac{-0.187 + 5.490 * 10^{-4} * T + 3.296 * 10^{-7} * T^2 - 8.261 * 10^{-11} * T^3}{100}, \quad (5.1)$$

where $\Delta L(= L(T)-L(293 \text{ K}))$ is the change in length relative to the room temperature length. In figure 5.2 is shown the calculated change in length caused by the thermal expansion alone and the total measured change in length for each individual XRD measuring temperature ($T_A-100^\circ\text{C}$). The difference between these two leaves us with the change in length caused by post radiation annealing. The curve suggests the decrease of the lattice parameter. This is in agreement with the expected behavior. The powder lattice parameter according to these calculations drops below its original unirradiated value already in the first anneal step at 300°C and afterwards keeps decreasing. In the upcoming section T_C is shown to have a full recovery at 350°C . According to these statements, the defects that are responsible for the a_0 change are different from those that are responsible for T_C change (anti-site defects). These new defects would have to have a very low activation energy. This however may be the result of the application of a thermal expansion that is not well fitted for our two-phase sample. This is supported by the fact, that after the final anneal step a_0 is equal to 5.275\AA , which is unexpectedly low. Improved measurements at the same temperature are necessary.

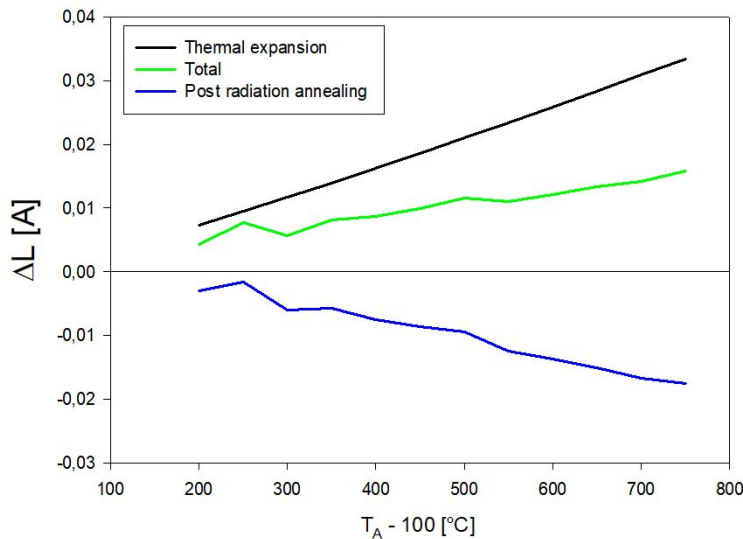


Figure 5.2: Change in length at different temperatures with different causes

5.2 Critical Temperature

$T_C^{10\%}$ and T_C^{onset} were derived from the data as described in section 4.4.1 for both samples. The critical temperature change with fluence and annealing temperature can be found in figure 5.3 obtained using the onset method and in figure 5.4 obtained using the 10% method.

Based on the plot a) in Appendix A, the measured T_C was lower than the T_C corresponding to 24.8 Sn at. %. The unirradiated sample contains naturally (not created through radiation) occurring defects, possibly regions of the measured second non superconducting phase Nb_6Sn_5 or the oxide NbO .

The powder sample was exposed to the highest fluence of $8.31 \cdot 10^{17}$ n/cm², which lead to a less than 0.6% decrease in T_C . The bulk sample was exposed to the highest fluence of $1.77 \cdot 10^{18}$ n/cm², which lead only to a less than 2% decrease in T_C . Both of the depressions at the given fluences are lower than what was previously reported [12].

Upon annealing up until 900°C a full recovery of T_C took place for both samples. The critical temperature T_C after the 900°C anneal shows even higher values than the T_C value of the unirradiated sample. The behavior of the critical temperature during annealing was observed to be very different for the bulk and powder sample.

T_C of the bulk sample increases very slowly up until 550°C and then increases rapidly. T_C^{onset} saturates around 700°C, whilst $T_C^{10\%}$ saturates only around 850°C. Different saturation temperature is simply a result of decrease in transition width ΔT , that will be addressed later on.

T_C increase of the powder sample at lower annealing temperatures is steeper than the increase of the bulk sample, but does not experience any evident change in slope as the bulk sample does at 550°C. T_C^{onset} saturates similarly to the bulk sample around 700°C, whilst $T_C^{10\%}$ has no visible saturation up until 900°C.

The following pages should give an insight into the different observed behavior upon annealing in the two samples.

In section 3.2 methods were introduced to describe the T_C vs. ϕ curve. A fit of the measured curves was performed to the Pande equation (3.4) extended by the Aronin equation (3.1):

$$\frac{T_C}{T_{c0}} = e^{-\alpha(1-e^{-k\phi})} \quad , \quad (5.2)$$

A two parameter fit (α and k) of this equation leads to inconclusive results, since both of

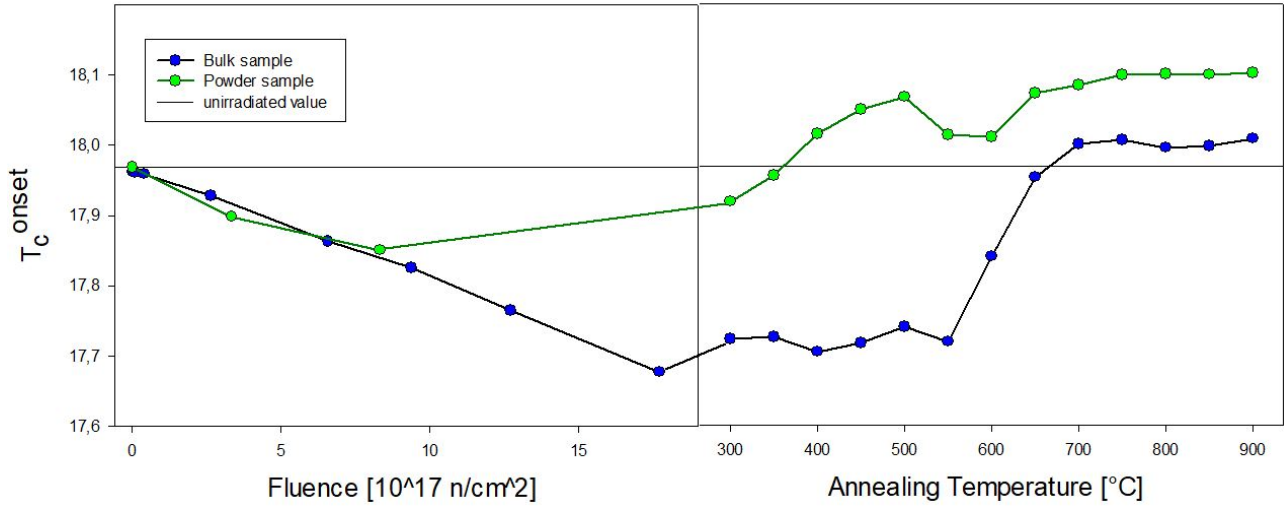


Figure 5.3: T_C^{onset} of the bulk and powder sample as it is being changed with fluence and annealing temperature

the parameters effect the fitted function in a similar manner. It is therefor necessary to determinate one of the parameters with a separate method. If precise measurements of the long range order parameter S from the X-ray diffraction were available, it would be possible to determinate k from Aronin. Due to the inconvenience of the transport of the radioactive material to a different institution after each irradiation step, in the present work X-ray diffraction was only performed after each anneal step, but not after each irradiation step necessary to calculate k . For that reason, one of the parameters had to be taken from the literature. The proportionality constant k is highly dependent on the used radiation beam energy and hence can not be taken from the literature. On the other hand the constant α is independent of radiation and is a material constant. Shiota also stated that the most accurate α , that could describe the full n range of T_C , is gained by fitting the Pande equation to T_C at $n=0$ and a n value above $10^{18}n/cm^2$. The highest fluence of $1.77 \cdot 10^{18}n/cm^2$ used in the present work seems to not be causing high enough damages on the lattice and therefore fitting α could lead to discrepancies. Retrieving α from the literature is a well considered decision. According to Shiota α for Nb_3Sn is around 5 ± 1.6 . For the purposes of this work α was established to be 5. The one parameter fit of the extended Pande equation for all four T_C vs. n curves can be found in table 4.

Table 4 also contains results gained from fitting the Hahn equation 3.3 and Bett equation 3.2. For comparison k was calculated for Hahn and Bett with $k = \beta/\alpha$. We observe that indeed all three equations result in a very similar k value, which can be ascribed to the use of low fluences. The observed k is an order lower than the values reported in section

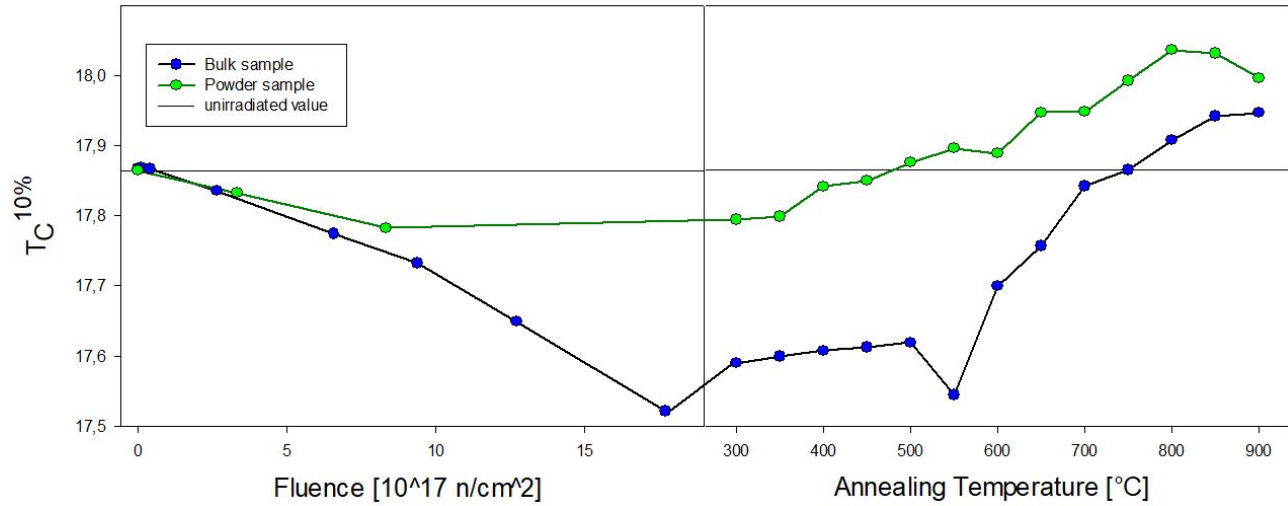


Figure 5.4: $T_C^{10\%}$ of the bulk and powder sample as it is being changed with fluence and annealing temperature

Sample	Curve	[10 ⁻²⁰ cm ² /n]				
		ex. Pande eq. 5.2	Hahn eq. 3.3		Bett eq. 3.2	
		k	β	k	β	k
Bulk	T_C^{onset} vs. n	0.1753	0.87545	0.17509	0.87013	0.174026
	$T_C^{10\%}$ vs. n	0.19928	0.99507	0.19901	0.98856	0.19771
Powder	T_C^{onset} vs. n	0.16933	0.84604	0.16921	0.84313	0.16863
	$T_C^{10\%}$ vs. n	0.11032	0.55138	0.11028	0.55023	0.11005

Table 4: Proportionality constant k obtained by fitting the extended Pande equation, Hahn equation and Bett equation.

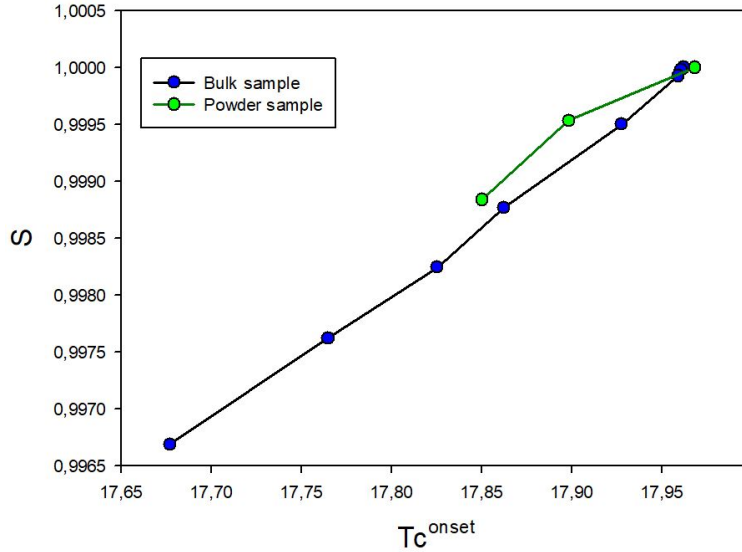


Figure 5.5: T_C^{onset} related to the long range order parameter S

3.1. The radiation source in the present work is causing less damage to the sample, less replacements per knock-on, than the radiation sources used in the references [12] and leads to lower decrease of T_C at the same fluence values.

Based on the assumption that the proportionality constant k could also be geometry dependent, from this moment on we will assume different values for the powder and bulk sample: $k_{Bulk}=0.18729 \cdot 10^{-20} \text{ cm}^2/\text{n}$ and $k_{Powder}=0.13983 \cdot 10^{-20} \text{ cm}^2/\text{n}$. These values are the average of the onset and 10% result of the extended Pande equation. Aronin equation 3.1 with the new k values will now be able to assign S to different T_C values. The resulting curves are visible in figure 5.5.

The powder sample does not have enough points to do so, but in the case of the bulk sample the S - T_C relationship can be fitted though a simple straight line. This line is a tool to assign the T_C values after annealing at different annealing temperatures to the long range order parameter. Plotting the resulting S against annealing temperatures should give us an insight of how the S parameter changes during annealing (figure 5.6).

Values of S above 1 responsible for T_C higher than the initial unirradiated value hint towards naturally (non-radiation induced) occurring defects in the sample, that got to be annealed out during the annealing process.

A function describing the change in S with annealing temperature in the same manner as the Aronin equation describes the change of S with fluence is still being searched for. The equation is bound to be more complex, consisting of more parameters than just the annealing temperature itself. This is evident from the non-identical behavior of T_C with

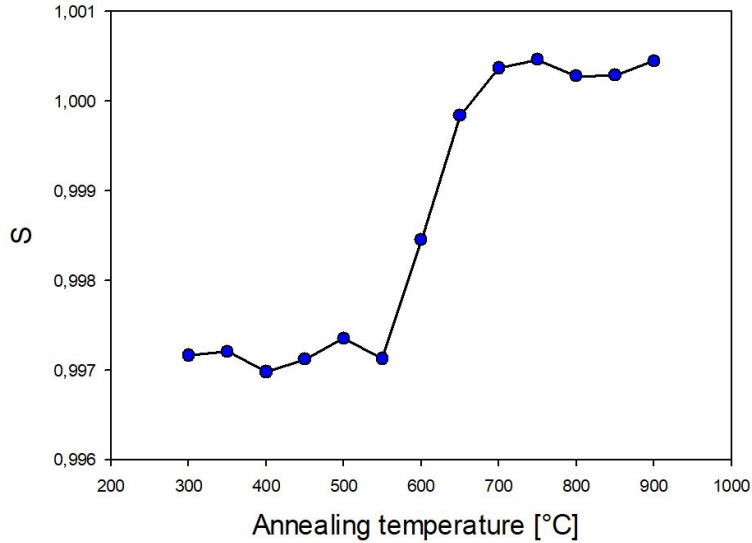


Figure 5.6: Long range order parameter S as it is being changed during annealing on the bulk sample

annealing temperature for the bulk and powder sample. The parameters that could be part of the equation, based on the results of the two samples, are the sample size and geometry and the different final fluence resulting in different activation energy.

- **Sample size and geometry**

A different T_C recovery behavior for the bulk and powder sample could be explained by their different surface areas. Considering that the radiation creates defects homogeneously throughout the sample, annealing of the defects could be happening from the surface inwards. The higher surface area of the powder sample would then lead to the mentioned quicker T_C recovery compared to the bulk sample. Observations of the transition width ΔT support this theory. The transition width is subtracted from the data as described in section 4.4.1 for both samples. The plot of the results divided by ΔT_0 , the unirradiated sample transition width, is seen in figure 5.7. As described in section 3.2, broadening of the transition width can uncover the existence of microregions in the sample, where T_C is different from the matrix. Looking at the present results it can be concluded that the change in transition width upon radiation is in the range of statistical error for both samples, hinting to homogeneously distributed defects and no microregions. Upon annealing one can observe a large difference between the behavior of the bulk and powder sample. Based on the present idea this could be explained followingly: as annealing of the defects starts at the surface, this leads to a difference in T_C between the surface and the inside of the bulk sample at lower annealing temperatures. At higher temperatures annealing reaches the full scale of

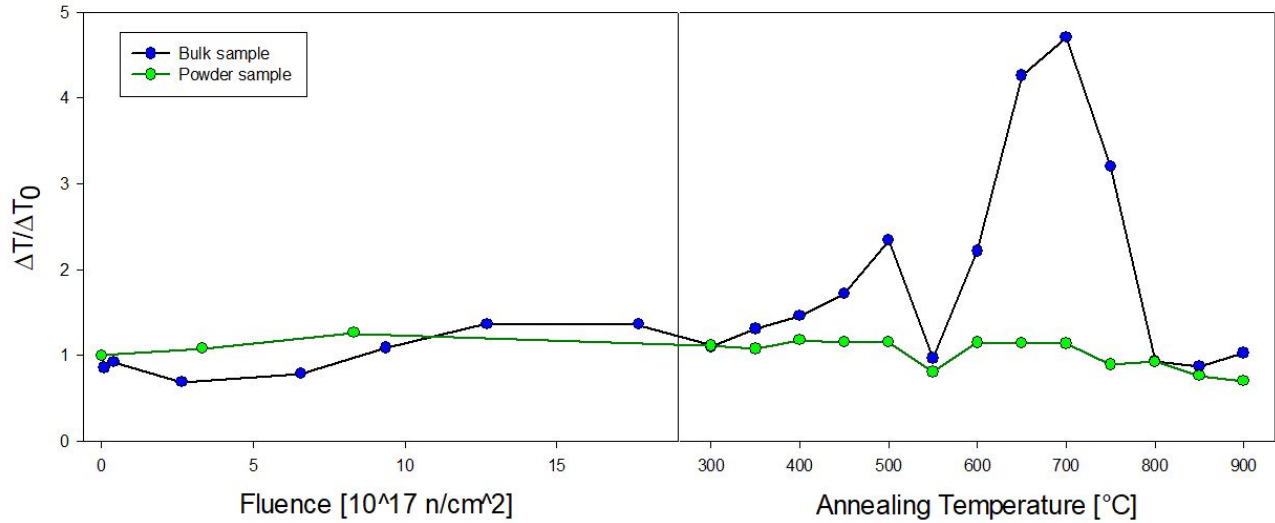


Figure 5.7: Transition width of the bulk and powder sample as it is being changed with fluence and annealing temperature

the sample and the sample returns to a homogeneously distributed state. The powder sample on the other hand indicates a homogeneously distributed state during its full annealing process, because the small sample size allows the annealing process to reach the inside of the sample even at low annealing temperatures.

- **Fluence**

The second idea explaining the different T_C recovery behavior for the bulk and powder sample is an idea based on activation energies introduced by Dew-Hughes. Section 3.2.1 describes the process of estimating the activation energies from T_C annealing data based on the plot of the equation 3.10. Dew Hughes plotted the T_C annealing data of two samples irradiated to two separate fluence values measured by Karkin et al [31, 22]. The results are plotted together with the present data in figure 5.8.

All three samples result in a two stage recovery curve. Dew Hughes however analysed the curves to be three stage curves of type b) from figure 3.2 with the low temperature stage missing. He based the statement on the fact, that the stage on the right indicated an activation energy around 0.6eV. This he claimed is too low to be only equal to the energy $U_R(A)$, but very reasonable to correspond to the energy $U_R(A)-U_M$. Three stage curves are typical for samples, where the count of initial vacancies is higher than equilibrium vacancies even at high temperatures. This seems like a very likely situation for irradiated samples. The idea is also supported by the plot of the bulk sample. Here the slope of the stage on the right is negative, which can only happen in the middle

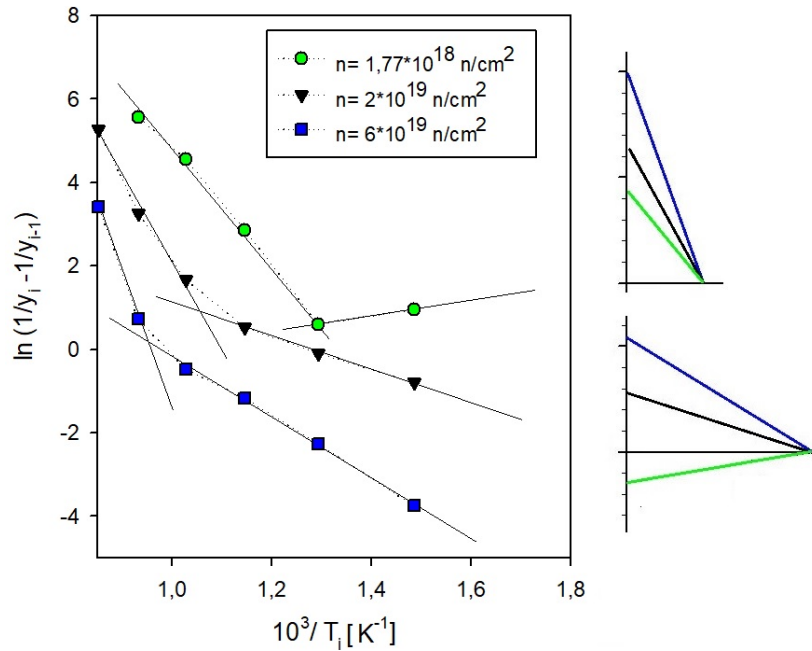


Figure 5.8: Plot of equation 3.10 for the bulk sample ($1.77 \cdot 10^{18} \text{ n/cm}^2$) and two samples measured by Karkin et al. The different slopes are highlighted by simple straight lines inside the plot. These lines are transferred on the right side to a single starting point for easier comparison. Upper slopes are slopes at higher temperatures, lower slopes at lower temperatures.

temperature stage. The absence of the low temperature stage might be caused by self-annealing during the irradiation process.

In figure 5.8, next to the plot, is a comparison of the slopes at higher and at lower temperatures. They both indicate that exposure to lower fluence will lead to less steeper slopes. A less steeper slope indicates lower activation energies and lower activation energy indicates quicker T_C recovery. The reason why exposure to lower fluence results in lower activation energies is not understood.

It should be noted that the samples in Karkin et al. [22] paper are described as parallelepipeds, but the exact measurements are not given. This prevents us from eliminating the possibility, that the different activation energy is actually only caused by different sample size and not by different fluence. We can only deduct that the two samples from Karkin et al. had the same size and these still indicate different activation energies. For the sake of this model we will consider it a fact, that the geometry is not a decisive parameter in the magnitude of the activation energy.

The powder sample was irradiated to a lower fluence than the bulk sample and according to this model the activation energies of the powder sample should be therefore

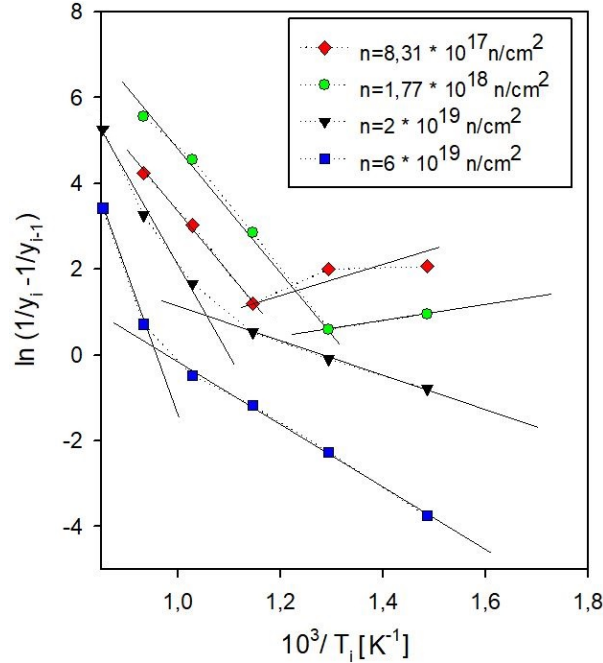


Figure 5.9: Plot from figure 5.8 extended by the powder sample with $n=8.31 \cdot 10^{17}$ n/cm²

lower. This would explain the quicker recovery in comparison to the bulk sample. A plot of the equation 3.10 for the powder sample is shown in figure 5.9. Whilst the middle stage still indicates lower activation energies than the activation energies for the bulk sample, the high temperature stage seems to have exactly the same activation energy as the bulk sample. According to the definition of the slopes, either the activation energy U_M or U_v is now higher for the powder sample than for the bulk sample.

Annealing experiments on different shaped samples irradiated to the same fluence, or same shaped samples irradiated to different fluences are fundamental to finding a correlation between the annealing temperature and S .

5.3 Upper critical field

The upper critical field of the bulk sample was derived from the data as described in section 4.4.2 for temperatures from 14.5K to 17.5K. These results were used to calculate the zero temperature upper critical field using multiple methods.

First, the data was fitted to the Maki de Gennes equation 4.1 with two fit parameters, T_C and $B_{C2}(0)$. The results are plotted in figures 5.10 and 5.11. As explained in section 3.3 upon irradiation it is expected for the upper critical field B_{C2} to grow. This is a consequence

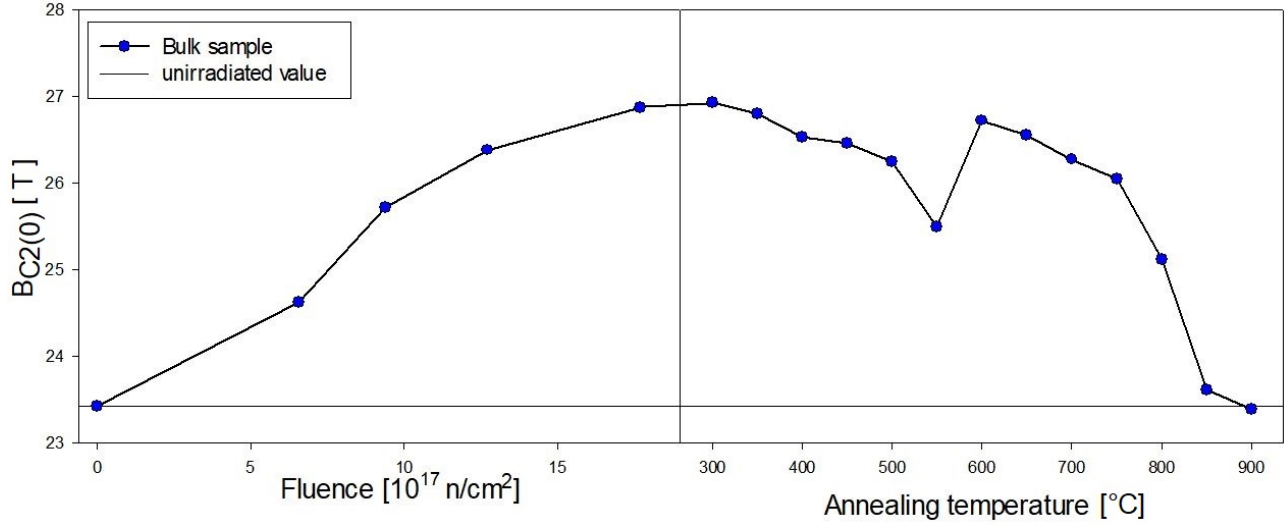


Figure 5.10: The zero temperature upper critical field of the bulk sample as it is being changed with fluence and annealing temperature, obtained by fitting the Maki de Gennes eq. 4.1

of the normal state resistivity growing faster than the critical temperature is dropping in equation 3.15. Similar consideration explains the shape of the curve upon annealing. At low annealing temperatures T_C growth is very subtle and the B_{C2} is dropping as the normal state resistivity is being lowered. At 550°C T_C suddenly starts to grow more rapidly, causing the B_{C2} curve to shift to higher values, but the curve still drops with the dropping normal state resistivity. Around 800°C, when the T_C^{onset} is saturated and $T_C^{10\%}$ slows down in its growth, B_{C2} experiences a rapid decrease with normal state resistivity as the decrease is no longer being suppressed by the T_C growth. At 900°C the B_{C2} value of the unirradiated sample is completely recovered.

The critical temperatures obtained during the Maki de Gennes fit are compared in figure 5.11 with the shape of the $T_C^{10\%}$ curve. It is concluded that their general shape is consistent. $T_C^{10\%}$ is a better representation of the overall critical temperature of the entire sample than T_C^{onset} .

In the second method, the WHH equation 4.4 utilizes the slope of B_{C2} in the vicinity of T_C . In order to calculate this slope from the measured data, the data was fitted to a straight robust line: $B_{C2}(T \lesssim T_C) = m T + b$, with m representing the slope $(dB_{C2}/dT)_{T \lesssim T_C}$ and b the intercept. The upper critical field is zero for $T = T_C$ and therefore $T_C = -b/m$. The WHH equation can now be written as: $B_{C2}(0) = -0.693 m T_C = 0.693 b$. $B_{C2}(0)$ was also calculated using the WHH equation and m for $T_C = T_C^{10\%}$, as $T_C^{10\%}$ seems to be a good representation of the critical temperature of the entire sample.

The straight robust line fit in the vicinity of T_C is a very big approximation, especially

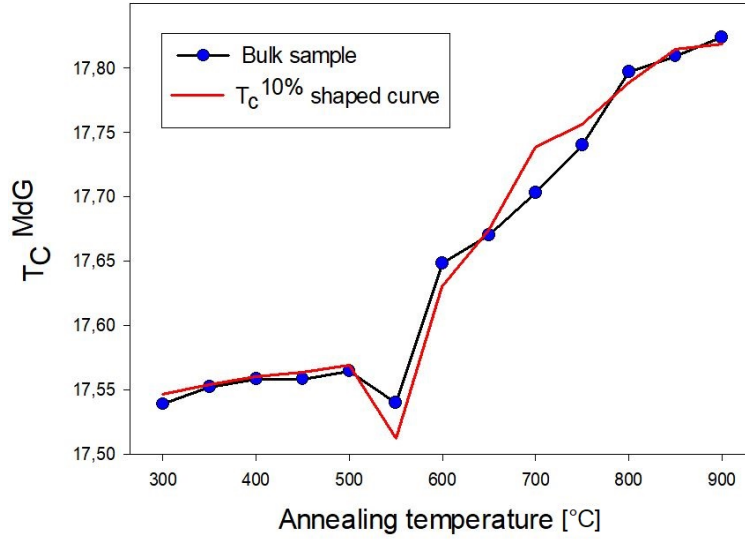


Figure 5.11: The critical temperature of the bulk sample as it is being changed with the annealing temperature, obtained by fitting the Maki de Gennes eq. 4.1

when fitting B_{C2} data for 17.5K all the way down to 14.5K. More accurate results can be achieved by substituting the slope in the more general WHH equation 4.2 by the slope from equation 4.4:

$$B_{C2}(T) = \frac{B_{C2}(0)}{0.693} h^*(t) \quad (5.3)$$

By fitting the numerically calculated values of $h^*(t)$ from the WHH paper [47], Baumgartner found the following description of the $h^*(t)$ equation [36]:

$$h^*(t) = 1 - t - 0.153(1 - t)^2 - 0.152(1 - t)^4; \quad t = T/T_C \quad (5.4)$$

In the vicinity of T_C the function $h^*(t)$ can be approximated to $1 - t$ and equation 5.3 can then be written as :

$$B_{C2}(T \lesssim T_C) = \frac{B_{C2}(0)}{0.693} - \frac{B_{C2}(0) T}{0.693 T_C} \quad (5.5)$$

Comparing this to the straight robust line fit: $B_{C2}(T \lesssim T_C) = m T + b$, $B_{C2}(0)$ can be calculated from b as previously mentioned.

Fitting the data, especially so far away from T_C , to equation 5.3 with the non approximated form of $h^*(t)$ from eq. 5.4 should provide the most accurate results.

Recovered data using all these different methods can be seen in figure 5.12. The previously described behavior of the curve in figure 5.10 is confirmed by the shape of all the other curves

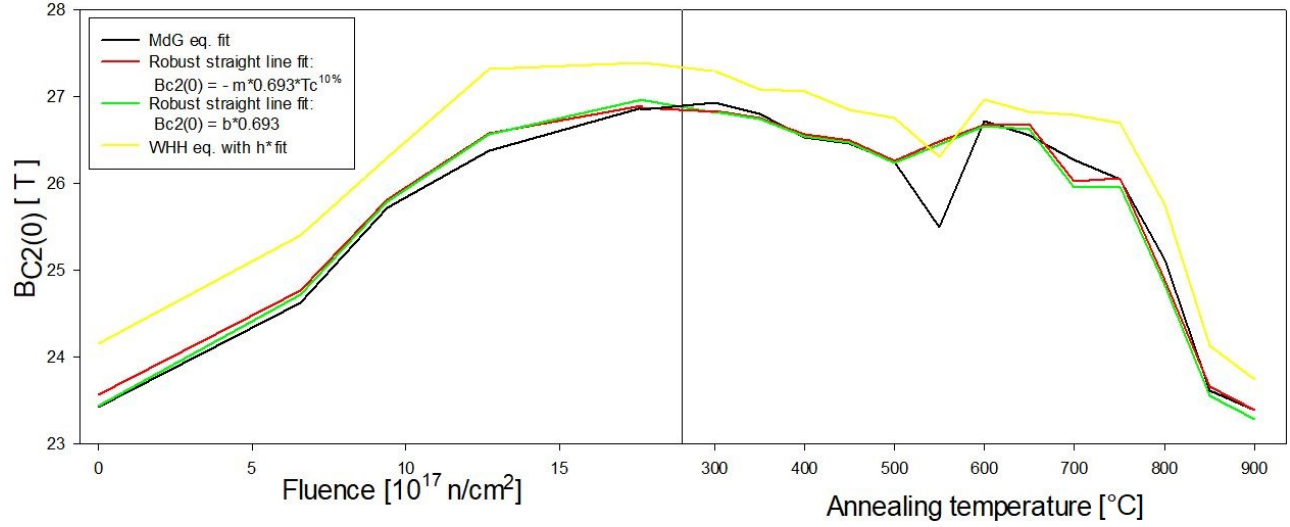


Figure 5.12: The zero temperature upper critical field of the bulk sample as it is being changed with fluence and annealing temperature. $B_{C_2}(0)$ was obtained using 4 different methods described in text.

as well. The measured critical temperature of the unirradiated sample corresponds according to the plot a) in Appendix A to a 24.5-24.8 at.% Sn content. The upper critical field of the unirradiated sample as read out from the plot b) in Appendix A for this Sn content predicts values between 24.5 and 26.6 T at $T=0K$. None of the curves predict a value this high, but fitting the WHH equation with the non approximated form of $h^*(t)$ (yellow curve) results in a curve that is bigger in magnitude than the rest, with $B_{C_2}(0)$ of the unirradiated sample being 24.15 T. This curve might be the most accurate representation of $B_{C_2}(0)$.

5.4 Penetration depth

The penetration depth of the bulk sample was obtained from the data as described in section 4.4.3. The SQUID MPMS data was fitted to a slightly modified version of the function 4.7. In place of radius a_n , were used values from the histogram presented in figure 4.2 and the expression is multiplied through their individual count rates. Since the histogram is only of a small portion of the sample, the summation has to be multiplied by a variable N .

$$m(T) = \left[\sum_n -\frac{H_0 a_n^3}{2} \left(1 - \frac{3\lambda(T)}{a_n} \coth \frac{a_n}{\lambda(T)} + \frac{3\lambda(T)^2}{a_n^2} \right) * count_n \right] N \quad , \quad (5.6)$$

where n is now the summation through the bins of the histogram. H_0 is equal to the amplitude of the alternating magnetic field, $30\mu T$ or $23.93A/m$. The penetration depth $\lambda(T)$ in equation 5.6 can be substituted through one of the three equations (4.9 - 4.11) to

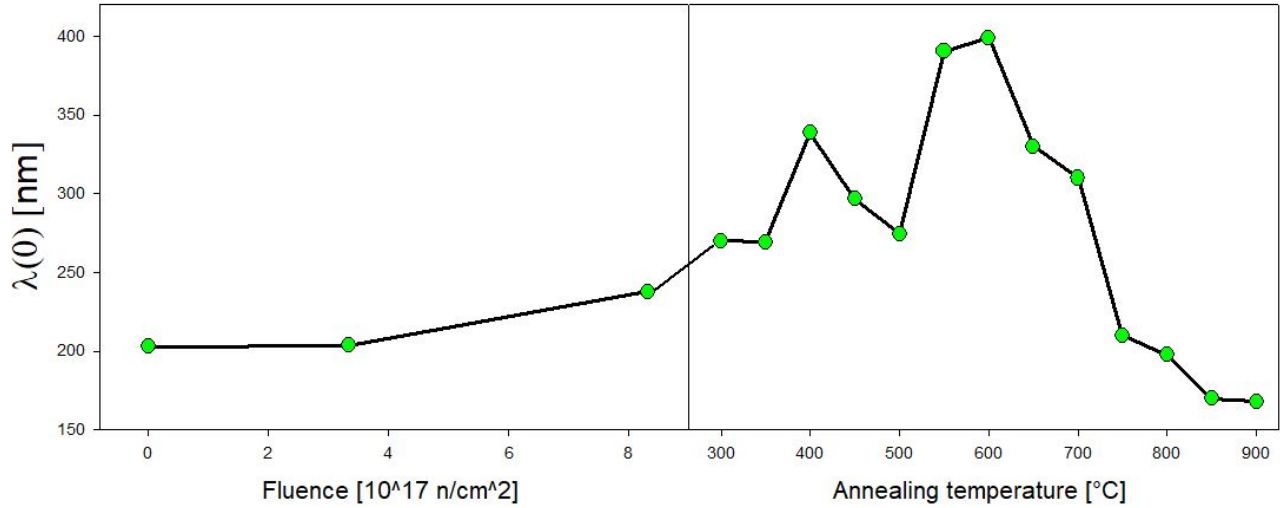


Figure 5.13: The critical temperature of the bulk sample as it is being changed with the annealing temperature, obtained by fitting the Maki de Gennes eq. 4.1

obtain information about the zero temperature λ .

For the Sn content 24.5-24.8 at.% corresponding to the measured T_C , the zero temperature penetration depth of the unirradiated sample according to plot d) in Appendix A should be between 107 and 117 nm. No matter which of the equations (4.9 - 4.11) is used in the fit, resulting value of $\lambda(0)$ is high above the mentioned values. The reason most probably being a high number of large grains in the powder, and a broad diversity in the shape of the grains. As mentioned in section 4.4.3, when using large grains in this measurement method, even small deviations in m lead to large errors in λ . For the diversity in shape can be accounted for, but also only if small grains are present. The radius of grains contributes to m with a^2 , so even a small number of large grains, that might not even be visible in the SEM image, will have a large effect on m .

For further fitting procedures it was decided to use the equation 4.11 in place of $\lambda(T)$ in equation 5.6, as it should be the most accurate relation. This leads to a three parameter fit, with the parameters $\lambda(0)$, T_C and N . N , correlated to the amount of grains in the powder, was left as a fitting parameter for all the steps of radiation and annealing, since the powder clung to the sides of the quartz tube and the amount of grains that were being measured changed. The results for the zero temperature λ are displayed in figure 5.13.

In section 3.4 it was predicted for the $\lambda(0)$ to grow with fluence. This behaviour was in fact observed. Upon annealing, $\lambda(0)$ should be dropping as a result of both the normal state resistivity ρ and the reciprocal critical temperature $1/T_C$ dropping. Instead, a step wise growth until 600°C is observed.

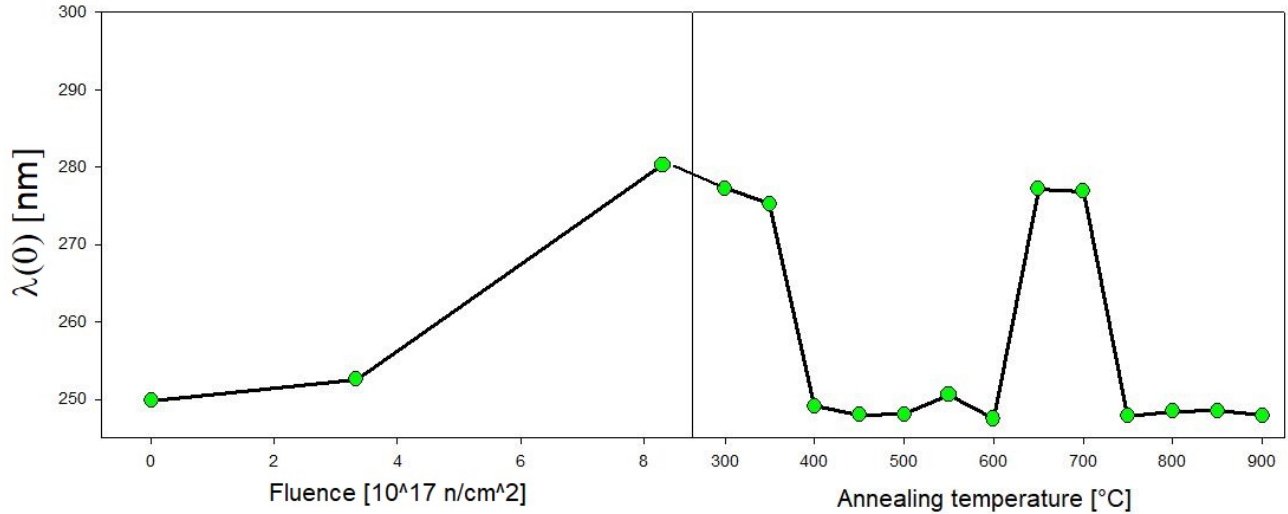


Figure 5.14: The critical temperature of the bulk sample as it is being changed with the annealing temperature, obtained by fitting the Maki de Gennes eq. 4.1

A new fit was performed to account for the different shapes in the powder as suggested by Waldram et al. [50] and described in section 4.4.3. This led to even more fitting parameters, since the exact number of spheres, rods and plates is unknown. The resulting curve of this procedure is in figure 5.14.

The results are so different from the previous fit, that it can be only concluded that it would be misleading to draw any kind of conclusion from these measurements. It has to be stated that to be able to correctly assess $\lambda(0)$ from MPMS SQUID measurements in the future, a sedimentation procedure to remove the large grains of the powder sample has to be made beforehand.

5.5 Critical current density

The critical current density of the bulk sample was derived from the data as described in section 4.4.4. The equation 4.14 was used to calculate $J_C(H)$. This was done for all radiation steps and annealing steps until 500°C annealing temperature. At higher annealing temperatures, after the cracking occurred, it was not possible to calculate $J_C(H)$, since the exact sample dimensions are required, and these were no longer known for the pulverized sample. For annealing temperatures above 500°C conclusions are drawn directly from the hysteresis loops.

Most of the hysteresis at 14K had many flux jumps, therefore to calculate J_C the hysteresis measured at 15K were used. The results are shown in figure 5.15. As described in section

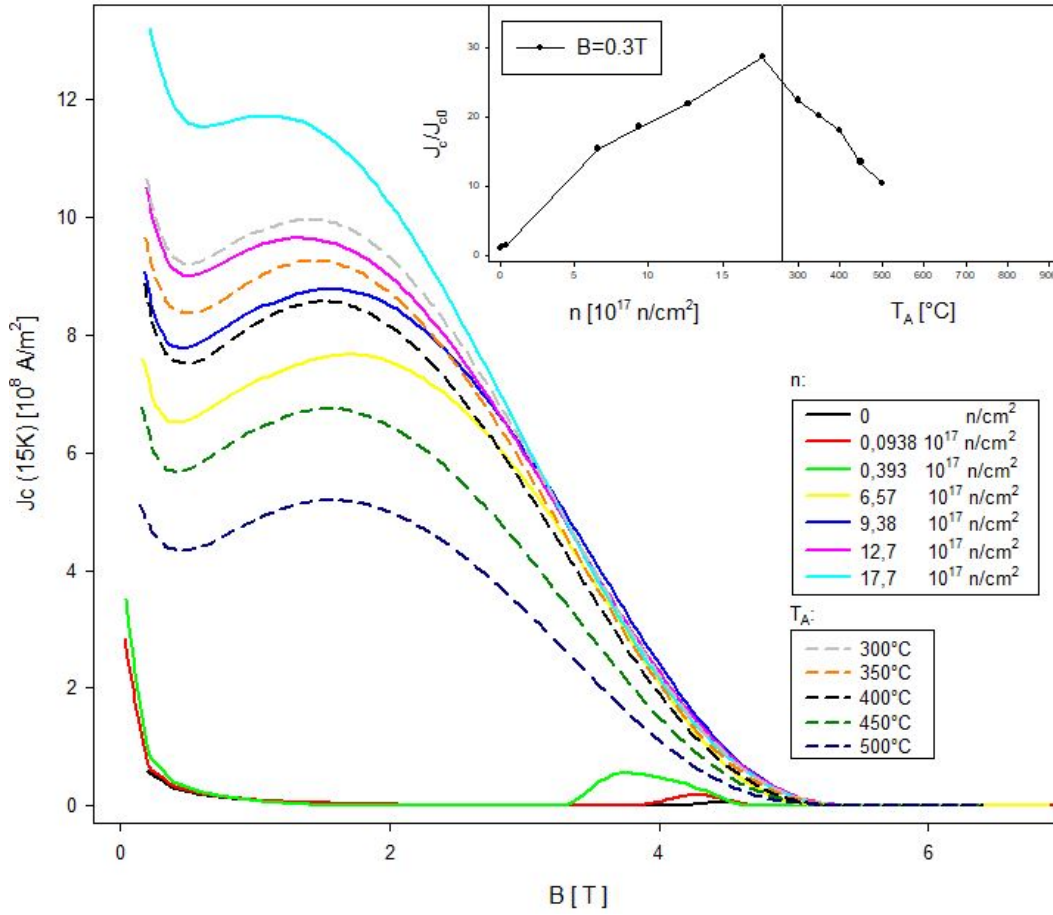


Figure 5.15: The critical current density $J_c(15K)$ of the bulk sample for different fluences and annealing temperatures

3.5, ΔJ_C is larger at low magnetic fields than at high magnetic fields, suggesting the critical current density being affected by the changes in point pinning force and irradiation induced defects acting as point pinning centers.

The insert in figure 5.15 is of J_C/J_{C0} plotted against fluence and annealing temperature at 0.3T applied field. The curve is increasing with fluence, but the described peak, after which a decrease should take place, is not reached. At the highest fluence J_C is enhanced by a factor of 29. Upon annealing J_C decreases abruptly and at 500°C declines 2/3 of the radiation achieved enhancement. Comparing this to the change in T_C , where T_C until 500°C experienced only a slight recovery, predicts the existence of a new radiation induced defect. Previously only the existence of anti-site defects responsible for change in T_C were discussed. These new defects effect pinning, but do not effect the critical temperature. They are annealed out at low temperatures, hinting to defects with lower activation energy than the anti-site defects.

The typical hysteresis shape for superconductors with defects, the fishtail shape, is reflected in the visible peak in $J_C(H)$ curve. Interestingly this peak is already present in the unirradiated sample around 4.4 T. This confirms the presence of the previously discussed natural occurring defects. As the fluence grows and therewith the defect density, the position of the peak moves to lower magnetic fields, corresponding to theory in section 4.4.4. The shift of the peak can be observed from hysteresis loops directly and its position can be specified even for annealing temperatures above 500°C. Figure 5.16 shows the field at which the peak occurs. The shape of this curve resembles the shape of $T_C^{10\%}$ from figure 5.4. This is not surprising as both parameters, T_C and the peak position, are effected by the defect concentration. A slight difference between the two curves though can be observed. The peak position seems to change more drastically at lower fluence than $T_C^{10\%}$, and the fast recovery step of the peak position starts only around 700°C, unlike around 600°C as is the case for $T_C^{10\%}$. This can be a consequence of a non-linear dependence of the peak position on the defect concentration. The position is more sensitive to low defect densities than to high defect densities.

In figure 5.4 $T_C^{10\%}$ at 750°C annealing temperature takes the same value as the unirradiated sample, however in figure 5.16 the field of the peak at 750°C is still way under the value of the unirradiated sample. This suggests an occurrence of radiation induced defects that do not affect T_C and have a higher activation energy than the anti-site defects.

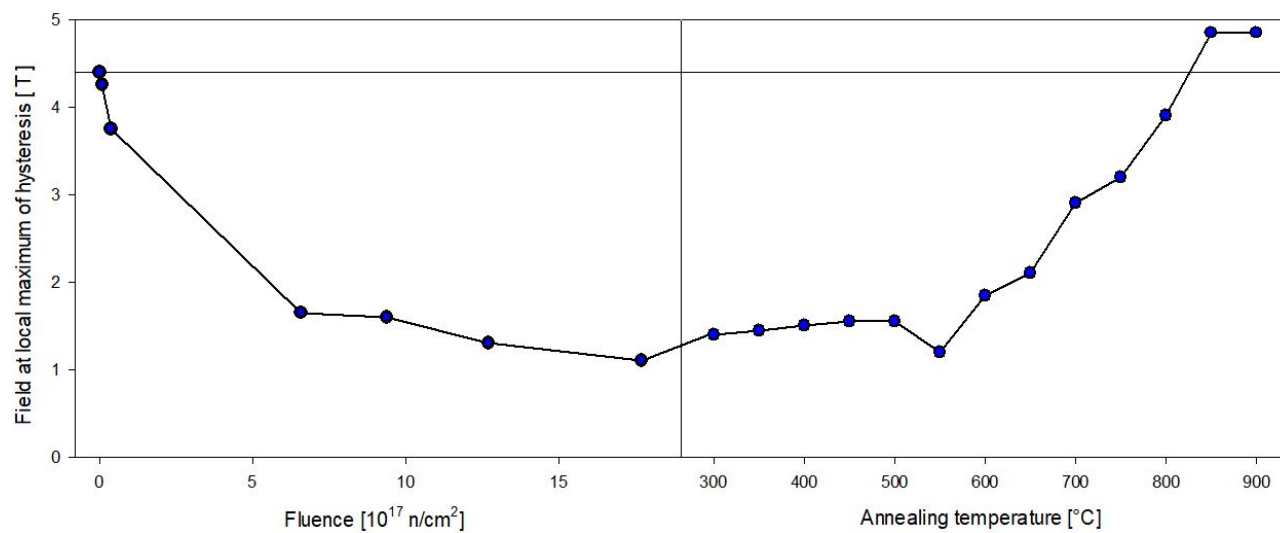


Figure 5.16: The field at which the local maximum of the hysteresis, measured at 15K, is located

6 Conclusion

The most important results can be summarized as follows:

- The unirradiated sample contained defects. These were visible in the XRD images and also confirmed through the effect they had on the critical temperature T_C and the critical current J_C . After annealing, T_C gained values above its unirradiated value and closer to the clean Nb_3Sn value, suggesting the defects being annealed out of the sample. The fishtail peak of the hysteresis similarly moves to magnetic fields higher than the fields for the unirradiated sample, however the existence of the peak at all highlights that the sample is still not clean of all defects. Whilst T_C is effected by the anti-site defects, critical current measurements hint to new defects with lower and with higher activation energies than the activation energies of the anti-site defects.
- Different recovery pattern of the T_C through annealing for the bulk and powder sample suggests a dependence on either the final fluence, the samples size or possibly both.
- The upper critical field after annealing was fully recovered to the value of the unirradiated sample and does not seem to be effected by the same defects as T_C and J_C .
- All changes on the superconducting properties caused by irradiation could be recovered by annealing.

The next steps in the research of the effects of neutron irradiation on Nb_3Sn should include measurements on same sized samples irradiated with different fluences or different shaped samples irradiated with the same fluence. During annealing the samples should be sealed in vacuum from the beginning to avoid cracking and oxidation. The XRD images of the annealing changes on the XRD pattern have to be performed at the same temperature to avoid having to take the thermal expansion into account. These measurements could then provide information not only about the lattice parameter, but also information about the long range order lattice parameter S as well. The measurements of the penetration depth on the powder sample should be tested again on a powder that has been through a sedimentation process to avoid any larger grains.

References

- [1] D. Dew-Hughes, "Flux pinning mechanisms in type II superconductors," *Department of Physics , University of Lancaster*, 1974.
- [2] G. Ambrosio, "Nb₃Sn high field magnets for the high luminosity LHC upgrade project," *IEEE Transactions on Applied Superconductivity*, vol. 25, pp. 1–7, 06 2015.
- [3] S. Pandolfi, "Once upon a time, there was a superconducting niobium-tin," <https://home.cern/news/news/engineering/once-upon-time-there-was-superconducting-niobium-tin>, JULY, 2016.
- [4] W. Schallreuter, *Grimsehl Lehrbuch der Physik IV*. 1975.
- [5] S. Buhler-Paschen, H. Michor, and M. Reissner, *Festkörperphysik I*. 2018.
- [6] S. Bühler-Paschen and P. Mohn, *Festkörperphysik II*. 2015.
- [7] P. Chaddah, "Critical current densities in superconducting materials," in *Sadhana Vol. 28, Parts 1 & 2, February/April 2003, pp. 273–282. Printed in India*, 2003.
- [8] S. Posen and D. L. Hall, "Nb₃Sn superconducting radiofrequency cavities: fabrication, results, properties, and prospects," *IOP Publishing- Superconductor Science and Technology, Volume 30, Number 3*, 2017.
- [9] A. S. Paul, T. Laurila, and V. Vuorinen, "Microstructure, Diffusion and Growth Mechanism of Nb₃Sn Superconductor by Bronze Technique," *DOI:10.5772/10118*, 2010.
- [10] Y. Li and Y. Gao, "GLAG theory for superconducting property variations with A15 composition in Nb₃Sn wires," *Scientific Reports*, vol. 7, apr 2017.
- [11] A. Goodeke, "A Review of the Properties of Nb₃Sn and Their Variation with A15 Composition, Morphology and Strain State," *Lawrence Berkeley National Laboratory*, 2006.
- [12] A. R. Sweedler, D. Cox, D. G. Schweitzer, and G. Webb, "Neutron induced disorder in superconducting A15 compounds," *IEEE Transactions on magnetics, vol. MAG -11, no. 2, march*, 1975.
- [13] C. Nölscher and G. Saemann-Ischenko, "Superconductivity and crystal and electronic structures in hydrogenated and disordered Nb₃Ge and Nb₃Sn layers with A15 structure," *Physical review B, vol. 32*, 1985.
- [14] R. Flükiger, *Atomic ordering, Phase Stability and Superconductivity in Bulk and Filamentary A15 type compounds*. Institut für Technische Physik, 1987.
- [15] R. Flükiger, T. Spina, F. Cerutti, A. Ballarino, C. Scheuerlein, L. Bottura, Y. Zubavichus, A. Ryazanov, R. D. Svetogovov, S. Shavkin, P. Degtyarenko, Y. Semenov, C. Senatore, and R. Cerny, "Variation of T_C , lattice parameter and atomic ordering in Nb₃Sn platelets irradiated with 12MeV protons: correlation with the number of induced frenkel defects," in *Supercond. Sci. Technol. 30 (2017) 054003 (11pp)*, 2017.
- [16] R. Aronin, "Radiation damage effects on order-disorder in Nickel-Manganese alloys," *Journal of Applied Physics 25, 344*, 1954.

- [17] A. Sweedler and D. Schweitzer, "Atomic ordering and superconductivity in high T_C A15 compounds," in *Physical review letters :volume 33, number 3* , 1974.
- [18] S. Shiota, S. Nishijima, and T. Okada, "Degradation of transition temperature and critical current density in neutron irradiated Nb_3Sn and V_3Ga ," in *IEEE Transactions on magnetics, vol. mag-17, No.1*, IEEE, 1981.
- [19] B. S. Brown, R. C. Birtcher, R. T. Kampwirth, and T. H. Blewitt, "Resistivity and T_C measurements in low temperature irradiated Nb_3Sn and Nb_3Ge ," *Journal of nuclear materials* 72, 1978.
- [20] O. Meyer and J. Pflüger, "X-ray diffraction studies on He - and Ar-irradiated Nb_3Ge thin films," *Solid state communications, vol 32*, 1979.
- [21] R. D. Burbank, R. C. Dynes, and J. M. Poate, "X-ray study of atomic displacements in Nb_3Sn induced by radiation damage," *Journal of low temperature physics, vol. 32*, 1979.
- [22] A. E. Karkin, V. E. Arkhipov, B. N. Goshchitskii, E. P. Romanov, and S. K. Sidorov, "Radiation effects in the superconductor Nb_3Sn ," in *Original Papers phys. stat. sol. (a) 38, 433*, 1976.
- [23] R. Meier-Hirmer, T. Reichert, and H. Kuepfer, "Critical current density and superconducting parameters T_c , H_{c2} and κ in neutron-irradiated and annealed V_3Si ," in *Transactions on magnetics, vol. mag-17, no. 1*, 1981.
- [24] R. Bett, "The effects of neutron irradiation induced atomic disorder on H_{c2} of Nb_3Sn ," *Cryogenics* 14, 7, 1974.
- [25] P. A. Hahn, M. W. Guinan, L. T. Summers, T. Okada, and D. B. Smathers, "Fusion neutron irradiation effects in commercial Nb_3Sn superconductors," *Journal of nuclear materials, 179 - 181*, 1991.
- [26] C. S. Pande, "A mechanism for the degradation of superconducting transition temperatures on high energy neutron irradiation in A-15 compounds," *Journal of Nuclear materials, 1978*.
- [27] J. A. Brinkman, "On the nature of radiation damage in metals," *Journal of Applied Physics* 25, 961, 1954.
- [28] S. Moehlecke, D. E. Cox, A. R. Sweedler, and J. Less, "Common metals, 62," *Solid state Communications* 23, 1977.
- [29] E. J. M. R. Flükiger, S. Foner, *Superconductivity of d and f Band metals (H. Suhl and M. B. Maple)*. Academic Press Inc., p. 265, 1980.
- [30] U. Schneider, G. Linker, and O. Meyer, "Superconductivity, structural disorder and phase transitions in ion-irradiated Nb_3Sn films," *Journal of low temperature physics, vol 47*, 1982.
- [31] D. Dew-Hughes, "Reordering kinetics of disordered A15 compounds," in *Phys. Chem. Solids Vol. 41, pp. 851-861*, 1979.
- [32] E. A. Lynton, *Superconductivity*. Methuen and Co. LTD, 1964.
- [33] L. P. Gorkov, "Theory of superconducting alloys in a strong magnetic field near the critical temperature," in *Soviet physics JETP vol. 37 (10), num. 5*, 1960.

- [34] C. L. Snead and D. M. Parkin, "Effect of neutron irradiation on the critical current of Nb₃Sn at high magnetic fields," *Nuclear Technology*, vol. 29, 1976.
- [35] H. Küpfer, R. Meier-Hirmer, and T. Reichert, "Field dependent change of the critical current density in neutron irradiated A15 superconductors with grain boundary pinning," *Journal of applied physics* 51, 1980.
- [36] T. Baumgartner, "Effects of fast neutron irradiation on critical currents and intrinsic properties of state-of-the-art Nb₃Sn wires," in *Dissertation University of Technology Vienna*, 2013.
- [37] B. S. Brown, T. H. Blewitt, D. G. Wozniak, and M. Suenaga, "Critical current changes in Nb₃Sn irradiated with fast neutrons at 6 K," *Journal of Applied Physics* 46, 5163, vol. 46, no. 12, pp. 5163–5168, 1975.
- [38] W. A. Fietz and W. Webb, "Hysteresis in superconducting alloys - temperature and field dependence of dislocation pinning in niobium alloys," *Physical Review* 178, 1969.
- [39] M. W. Guinan, R. A. van Konynenburg, and J. B. Mitchell, "Effects of low-temperature fusion neutron irradiation on critical properties of a monofilament niobium-tin superconductor," *Lawrence Livermore national library*, 1984.
- [40] T. Baumgartner, M. Eisterer, H. W. Weber, R. Flukiger, B. Bordini, L. Bottura, and C. Scheuerlein, "Effects of neutron irradiation on pinning force scaling in state of the art Nb₃Sn wires," *Superconductor science and technology*, vol. 27, 2014.
- [41] T. Spina, "Proton irradiation effects on Nb₃Sn wires and thin platelets in view of High Luminosity LHC upgrade," in *Dissertation at CERN, European Organization for Nuclear Research, Geneva*, 2015.
- [42] M. McElfresh, *Fundamentals of magnetism and magnetic measurements featuring Quantum Designs Magnetic Property Measurements system*, 1994.
- [43] "Magnetic property measurement system - AC option users manual," in *Quantum Design*, 1999.
- [44] P. G. de Gennes, "Behavior of dirty superconductors in high magnetic fields," *Physik der kondensierten Materie*, 1964.
- [45] K. Maki, "The magnetic properties of superconducting alloys. II," *Physics Vol. 1, No. 2*, pp. 127-143, 1964.
- [46] A. Godeke, H. H. J. K. B. Haken, and D. C. Larbalestier, "A general scaling relation for the critical current density in Nb₃Sn," *Superconductor Science and Technology*, Volume 19, Number 10, 2006.
- [47] N. R. Werthamer, K. Helfand, and P. C. Hohenberg, "Temperature and Purity Dependence of the Superconducting Critical Field, III. Electron Spin and Spin-Orbit Effects," *Physical review vol. 147, n. 1*, 1966.
- [48] T. P. Orlando, E. McNiff, S. Foner, and M. Beasley, "Critical fields, pauli paramagnetic limiting and material parameters of Nb₃Sn and V₃Si," in *Physical review B*, vol. 19, num. 9, 1979.
- [49] D. Shoenberg, *Superconductivity*. Cambridge university press, 1960.

- [50] J. R. Waldram, A. Porch, and H. M. Cheah, "Measurement of the microwave conductivities of high- T_C superconducting powders," *Physics C* 232, 189-198, 1994.
- [51] J. G. Daunt, "Temperature dependence of penetration depth of a magnetic field in superconductors," *Letters to the editor*, 842, 1948.
- [52] R. Prozorov and R. Giannetta, "Magnetic penetration depth in unconventional superconductors," *Superconductor science and technology*, 2006.
- [53] D. A. Bonn, P. Dosanjh, R. Liang, and W. N. Hardy, "Evidence for Rapid Suppression of Quasiparticle Scattering below T_C in $\text{YBa}_2\text{Cu}_3\text{O}_7$," *Physical review letters* vol. 68, num. 15, 1992.
- [54] C. P. Bean, "Magnetization of high-field superconductors," *Review of modern physics*, 1964.
- [55] A. Nabialek, M. Niewczas, H. Dabkowska, and A. Dabkowski, "Magnetic flux jumps in textured $\text{Bi}_2\text{Sr}_2\text{CaCu}_2\text{O}_{8+\delta}$," *Physical review B* 67, 2003.
- [56] M. Zehetmayer, "How the vortex lattice of a superconductor becomes disordered: a study by scanning tunneling spectroscopy," *Scientific reports*, 2015.
- [57] M. Zehetmayer, M. Eisterer, J. Jun, S. M. Kazakov, J. Karpinski, B. Birajdar, O. Eibl, and H. W. Weber, "Fishtail effect in neutron-irradiated superconducting MgB_2 single crystals," *Physical review B* 69, 2004.
- [58] M. Lopez, J. A. Jimenez, K. Ramam, and R. V. Mangalaraja, "Synthesis of nano intermetallic Nb_3Sn by mechanical alloying and annealing at low temperature," *Journal of alloys and compounds* 612, 215-220, 2014.
- [59] N. Mitchell, "Finite element simulations of elasto-plastic processes in Nb_3Sn strands," *Cryogenics* 45, 501-515, 2005.
- [60] D. Gajda, A. Zaleski, and A. Morawski, "New types of high field pinning centers and pinning centers for the peak effect," *Superconducting science and technology* 30, 2017.

A Superconducting properties of Nb₃Sn as functions of Sn content

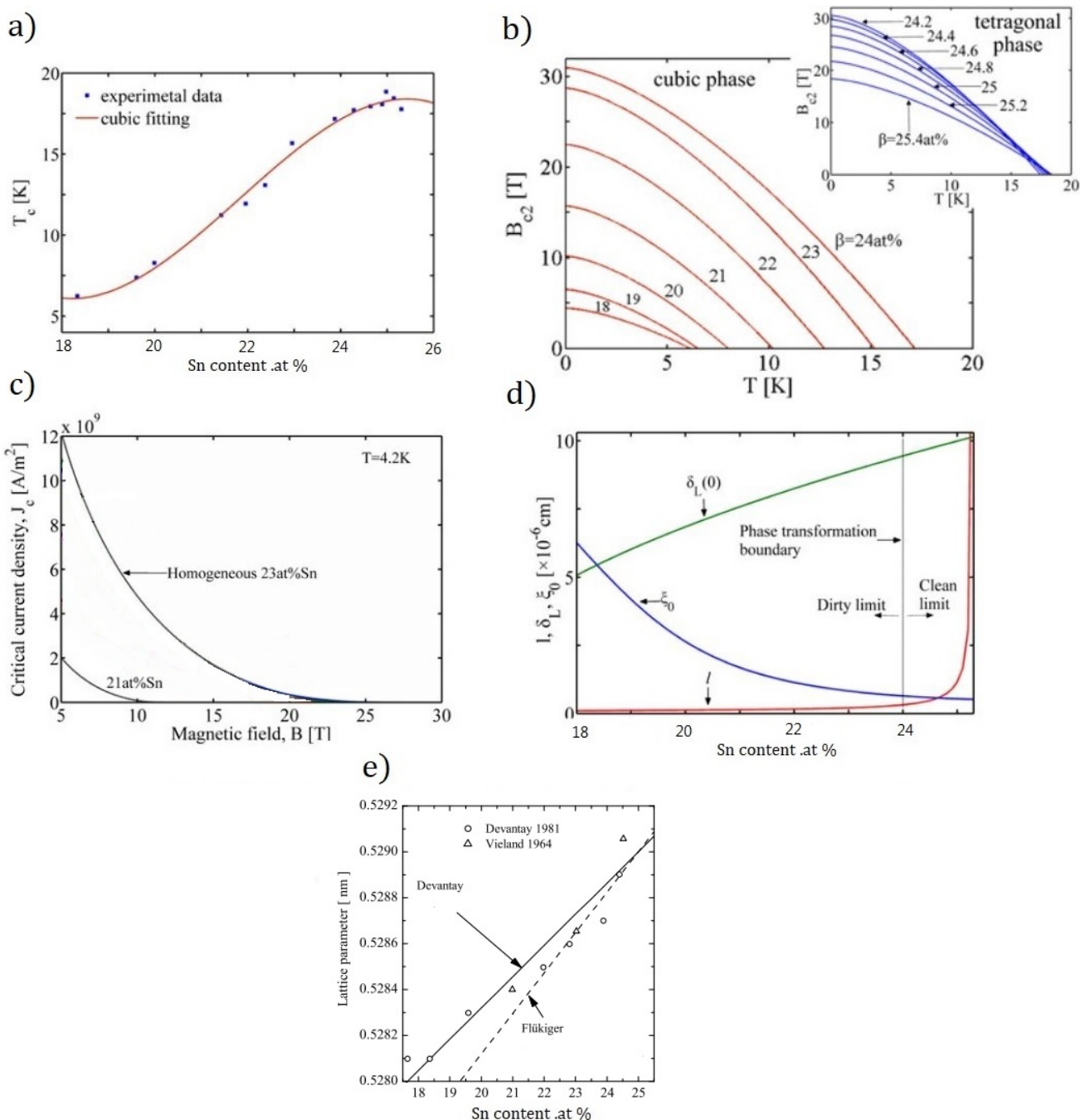


Figure A.1: [10, 11] a) Critical temperature vs Sn at. %; b) Upper critical field vs. temperature for different Sn at.%; c) Critical current density vs. field for 21 and 23 Sn at. %. The absolute value of J_C is dependent on the samples geometry; d) Mean free path l , London penetration depth $\lambda_L(0)$ (δ_L in figure) and coherence length ξ_0 vs. Sn at.% (note that the effective penetration depth $\lambda(0)$ is equal to $\lambda_L(0)(\xi_0/l)^{1/2}$ in the dirty limit); e) Lattice parameter vs. Sn at.%

B SQUID

A SQUID consists of a superconducting ring with two Josephson junctions (J.J.) as pictured in figure B.1. As introduced in subsection 2.1.2, magnetic flux inside a superconducting ring Φ_{in} is quantized, meaning only an integer quantum can exist inside of the ring. Plots a) and b) in figure B.1 can be therefor understood followingly: until the value for the outside field reaches half a quantum, screening current J will screen the outside field from the inside of the ring. After half a quantum is reached, it is energetically favorable to let the outside field inside the ring and reverse the current J to create a field inside the ring that will add up with the outside field to a full quantum. The current J changes direction every time half a quantum is added, therefore the periodicity T is equal to one flux quantum. Plot c) explains how this process effects the value of the critical current of the SQUID, considering I_A to be the critical current of a single J.J. The J.J. is a very thin insulator layer ($\approx 30 \text{ \AA}$) that can pass supercurrent without resistance. Once the current is higher than its critical value, a voltage appears. Plot d) shows the voltage of a SQUID that passes the current I . The curve in plot d) is dependent on the value of the outside magnetic field. For a constant I the voltage is periodic with changing flux as shown in plot e). Measuring a change in voltage across the SQUID will give information about the change in magnetic flux. On the other hand if the magnetic flux is constant a SQUID can be used as a current to voltage converter.

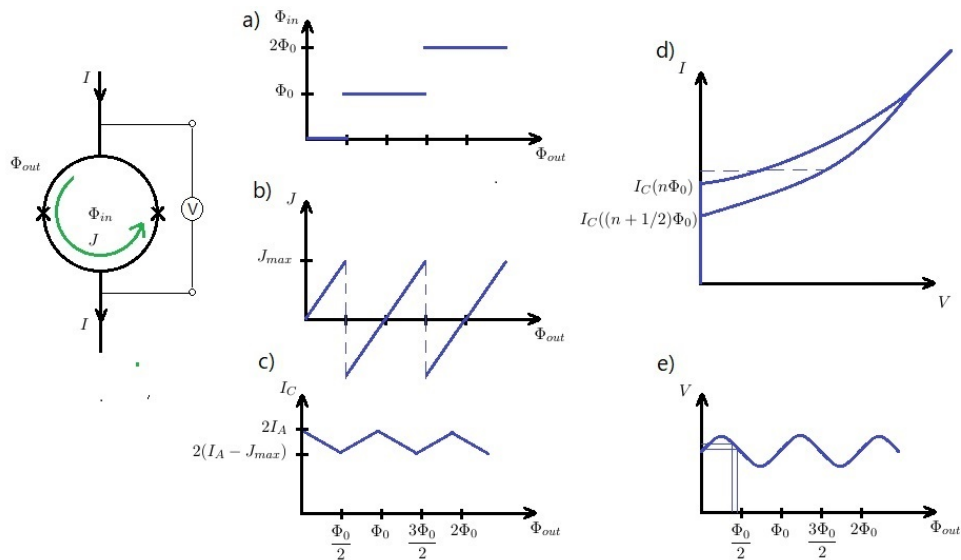


Figure B.1: Left is a diagram of a SQUID where x represents the Josephson junctions.